Photoluminescence Spectroscopy of BiI_3, a 2D Material for Photovoltaic Applications

A Major Qualifying Project Submitted to the faculty of

WORCESTER POLYTECHNIC INSTITUTE

in partial fulfillment of the requirements for the
Degree in Bachelors of Science
in

PHYSICS

By
ALEXIS BUZZELL & ANDREW MENDIZABAL

4/25/19

Project advisor:
Professor Lyubov Titova

Abstract

Many two-dimensional (2D) semiconductors show promise for photovoltaic applications due to their desirable bandgap (1-3 eV) resulting in high absorption in the visible range, predicted long charge carrier lifetimes, and high carrier mobility. In addition, many, 2D semiconducting materials are composed of nontoxic and earth abundant elements, and can be fabricated into thin, lightweight and flexible devices. One of the candidate 2D solar energy materials is bismuth triiodide (BiI_3), which has a bandgap of 1.67 eV and is anticipated to be defect-tolerant as predicted defect states are shallow and should have detrimental effect on carrier lifetime. In this project, we have used spectrally- and time-resolved photoluminescence spectroscopy to study optical properties and radiative carrier lifetime in bulk single crystal BiI_3. To achieve this goal, we have implemented and characterized a time-resolved photoluminescence spectroscopy setup using time-correlated single photon counting (TCSPS) technique. We attribute the main photoluminescence peak with energy of 1.82±0.01 eV and radiative lifetime in the range of 240-300 ps to a free exciton. In addition, we observe a weaker emission due to indirect bandgap recombination at 1.68±0.01 eV. Most importantly, we find that optical properties are uniform across the crystal surface, and visible surface defects only modulate overall intensity but have no influence over the emission spectra or radiative lifetime. Future work will correlate these results with time-resolved terahertz spectroscopy in order to get a complete picture of photoexcited carrier dynamics.

Acknowledgements

Thank you, Professor Titova, for all of your help in guiding us through this project and helping us overcome all the challenges we faced.

Thank you, Kateryna Kushnir and Dr. Teng Shi, for help troubleshooting and providing your expertise in the lab, as well as helping us practice our presentation.

Thank you, Patrick Fitzgerald, for providing insight to spectrometer operations.

Thank you, Benjamin Child, Nathaniel Mione, Erin, Morissette, Taylor Trottier, and Bryannah Voydatch for listening to and providing insight on our practice presentations.

Thank you, Professor Grimm and Julia Martin, for supplying samples of BiI_3 for us to test.

Table of Contents

Table of Figures

Table of Tables

Chapter 1: Introduction and Background

In semiconductors and insulators, occupied energy levels of the valence band and unoccupied energy levels of the conduction band are separated by the bandgap, where no allowed states exist. When a semiconductor absorbs light with photon energy that is equal to or greater than the bandgap, electrons are promoted from the valence to the conduction band, allowing them to flow through the material as electrical current. (Hoang, 2008; Smith, 2010). Semiconductors are thus uniquely capable of converting light into electricity, making them essential components of photovoltaic and photoelectrochemical devices. While the most common material in solar cells at this time is silicon, the search is ongoing for alternatives that requires less energy to produce, and is efficient, non-toxic and comprised of earth abundant elements. Two-dimensional (2D), or van der Waals, semiconductors include many potential candidates for efficient photovoltaics (Castellanos-Gomez, 2016, Xia et al., 2014, Poole, n.d.). In 2D materials, layers of single-atom or few-atom thickness are held together by weak van der Waals forces (Xia et al., 2014, Xu et al., 2013). Electrons can easily move within each associated layer but interlayer electronic transport is suppressed, making 2D materials inherently nanostructured.

In this paper, we focus on the optical properties of one 2D semiconductor material, bismuth triiodide (BiI_3). BiI_3 not only has many characteristics necessary for solar cell materials (bandgap in the visible range, flexibility, relative ease of processing) but is also predicted to be highly tolerant to defects, making it a very attractive photovoltaic material (Scholtz, Oum, & Lenzer 2018; Brant et al., 2015; Tiwari, Alibhai, & Fermin, 2018).

To study the optical properties of BiI_3 we used spectrally- and time-resolved photoluminescence spectroscopy. Photoluminescence is emission of light by the sample that has been optically excited, typically, with a laser beam. Analyzing this optical emission yields important information about energy landscape and radiative lifetime of the charge carriers.

Our first goal was to establish a system capable of time-resolved photoluminescence spectroscopy. To this effect, we have added a ~50 ps duration pulsed laser, a fast avalanche photodiode (APD) and electronics for time-correlated single photon counting to an existing photoluminescence spectroscopy system that allowed measurement of photoluminescence spectra using a combination of an imaging spectrometer and a charge-coupled device (CCD). We have characterized the new setup and were able to validate it using known samples: molybdenum disulfide (MoS_2) monolayers and cadmium selenide (CdSe) quantum dots.

Finally, we had carried out extensive measurements of spectrally-, power- and time-dependent photoluminescence of BiI_3 single crystals grown in the laboratory of Professor R.L. Grimm using sublimation. We find that emission energy and radiative lifetime varies very little across the sample, with visible surface defects only affecting overall emission intensity. We attribute the main emission peak to recombination of direct gap excitons, and an additional broad low energy shoulder to recombination of free electrons and holes across the indirect bandgap. In future measurements, we will correlate radiative carrier recombination to the lifetime of the free carriers as measured by the time-resolved terahertz (THz) spectroscopy (Peiponen, Zeitler, & Kuwata-Gonokami, 2013) and study the effects of surface oxidation on optical properties.

1.1 Two-Dimensional Materials

A material is classified as a nanomaterial when at least one dimension is 500 nanometers or smaller in size (Edvinsson, 2018). In the past decade, nanomaterials have been of interest for

research due to the capability to tune their electronic, optical, and other physical properties (Xu et al., 2013, Hsueh, Li, & Ho, 2018). Constraining spatial dimensions of a material to the nanoscale results in quantum mechanical confinement effects that manifest themselves in electronic properties and optical transitions that are different from the same material in bulk (Xia et al., 2014, Hsueh et al., 2018). Size-dependent changes can be explained by the change in band structure of the material as the size is altered, as will be further discussed in Section 1.2. Reducing the size of the material also causes an increase in the surface area to volume ratio of the structure (Roduner, 2006; Xu et al., 2013). Many applications require physical interactions and/or chemical reactions at the surface for device operation, making nanomaterials advantageous due to their increased surface area (Rao, 2019). Applications that require a large surface area include energy conversion, energy storage, and chemical sensing. However, confining dimensions and increasing surface area can be undesirable because surfaces often create defect states that trap electrons, and increased electron scattering and shorter mean free path are a result of smaller structure size (Zhang, Uchaker, Candelaria, & Cao, 2013). The major research goal in the material science community is fabrication of nanostructured materials with optimized and tuneable electronic and optical properties for desired application while also minimizing adverse effects that inhibit device operation (Gupta et al., 2015).

1.2 Semiconductors

Semiconductors can be distinguished from other materials such as metals or insulators by the structure of their electronic energy levels (Callister, 2014, Introduction to Semiconductors, 2009). Semiconductors have an occupied valence band state and, at low temperatures, an empty conduction band state (Jenkins, 2005, Sze, 2007, Seeger, 1999). An energy gap, known as the bandgap, where electrons are quantum mechanically forbidden to exist, separates the valence band and conduction band (Callister, 2014, Hoang, 2008). Semiconductors can have bandgaps in the range of 1 to 3 eV, and therefore photons from visible or UV light have sufficient energy to promote an electron from the valence band to the conduction band. This process is known as inter-band optical excitation and is responsible for many optoelectronic properties in semiconductors.

When an electron is promoted to the conduction band following absorption of a photon with sufficiently high energy, an empty state is left in place of the electron in the valence band. This empty state behaves like a positively charged carrier and is called a hole. If the Coulomb interaction between the electron and hole is sufficiently strong, it can result in the creation of a hydrogen-like bound state called an exciton (Hoang, 2008, Fox, 2001 Yu & Cardona, 2010). An exciton is stable at room temperature if its binding energy, calculated as follows:

$$E_b = \frac{e^2}{\varepsilon a_0^*} = \frac{e^2 a_0}{(m^*/m)(a_0^*)^2} \quad (1)$$

$$a_0^* = \frac{m}{m^*}\varepsilon a_0 \quad (2)$$

is larger than the thermal energy (kT=25.7 meV) (Dvorak, Wei, & Wu, 2013). Where m and m^* are the electron mass and electron effective reduced mass, a_0 is the Bohr radius of the hydrogen atom, e is the electron charge, and ϵ is the dielectric constant (Dvorak et al., 2013). The electron-hole pair will eventually recombine, either non-radiatively or radiatively. When non-radiative recombination occurs energy is released by emitting phonons or releasing energy into the lattice structure. Radiative recombination, also known as photoluminescence, will be discussed in detail in Section 1.4.

Semiconductors can be classified as having a direct or an indirect bandgap. In a direct bandgap, the minimum energy value of the valence band and the maximum energy value of the conduction band both occur at the same wave-vector (***k***) value, as seen in Figure 1 (a). An indirect bandgap occurs when the extrema of the valence and conduction band occurs at different wave-vector values, as seen in Figure 1 (b).

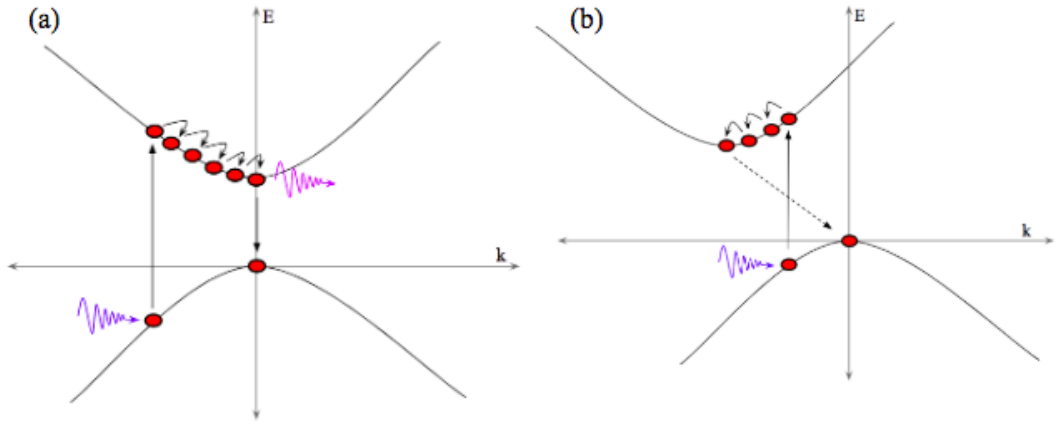

Figure 1: a) Photoluminescence process in a direct bandgap semiconductor material b) Photoluminescence process in an indirect bandgap semiconductor material: as initial and final states of an electron have a different wave-vector (momentum), momentum conservation requires that a large momentum phonon is involved in this process

1.3 Bismuth Triiodide

In the last decade, solution processed photovoltaics based on hybrid lead halide perovskites have attracted much attention due to their exceptionally high (>20%) conversion efficiencies (Scholz et al., 2018; Brant et al., 2015). However, their instability and lead content has raised environmental concerns, and the search for new materials to replace lead halide perovskites in solution processable, efficient solar cells has resulted in a focus on bismuth-containing semiconductors instead such as BiI_3 and BiOI (Scholtz et al., 2018, Brant et al., 2015, Tiwari et al., 2018, Hamdeh et al., 2016). Bismuth is nontoxic, and bismuth compounds are more stable compared to lead halide perovskites (Scholtz et al., 2018; Brandt et al., 2017).

Bismuth triiodide (BiI_3) has been gaining attention in particular because of its bandgap in the visible range that would make it a useful top material for a multijunction solar cell (Brant et al., 2015). A range of bandgaps have been found experimentally and computationally between 1.43 eV and 2.2 eV (Podraza et al., 2013). Both direct and indirect bandgaps have been reported in theoretical investigations using density functional theory as well as in experimental studies. Experiments yield the direct bandgap at 1.97 eV and the indirect bandgap to be 1.67 eV (Podraza et al., 2013). Known properties of BiI_3 that are relevant to its photovoltaic performance are summarized in Table 1. The structure of BiI_3 is composed of a layer of bismuth stacked between two layers of iodide, and van der Waals forces holding these trilayer sheets together, as shown in

Figure 2 (Yan et al., 2018). The stacking of these layers occurs in a nearly hexagonal close packed lattice (Scholz et al., 2018). Monolayers of BiI_3 are achieved by exfoliating the individual trilayers and breaking the van der Waals forces between them.

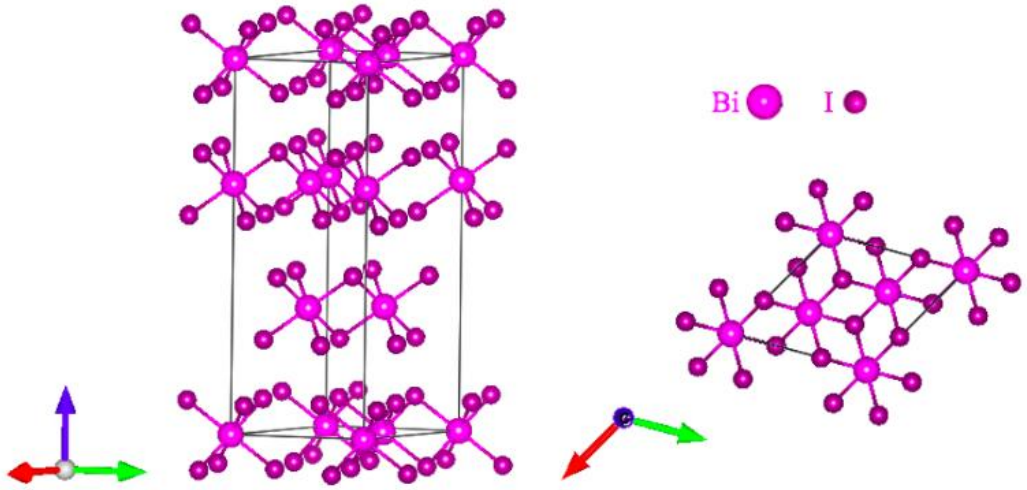

Figure 2: BiI_3 crystal structure

Table 1: BiI_3 Characteristics

BiI_3	Values	Note
Crystal Structure	Rhombohedral Space Group R3, No. 148 Z = 6	Room Temperature (Podraza et al., 2013)
Bandgap	1.43-2.2 eV	Direct and Indirect (Podraza et al., 2013)
Electron Mobility	260 ± 50 $cm^2/(V\cdot s)$ 1000 ± 200 $cm^2/(V\cdot s)$	 with Sb-doping (Brendt et al., 2015)
Minority Carrier Lifetime	1.54 ns	(Tiwari et al., 2018)
Resistivity	10^8 to 10^9 Ω-cm	(Brendt et al., 2015)
Density	5.78 g/cm^3	(Shen & Wang, 2017)

However, a decrease in energy efficiency is one concern with replacing lead-based materials with bismuth-based materials in photovoltaics. Desirable energy conversion efficiencies to justify replacing lead-containing photovoltaics with bismuth-containing ones is at least 20% (Brant et al., 2017). Charge carrier lifetime, or the time it takes for a minority carrier to recombine, is an important parameter in energy efficiency. In order for a solar cell to produce energy, charge carriers must be generated and escape the solar cell, and the probability of this

event increases with longer carrier lifetimes (Poindexter, 2018). While >100 nanosecond lifetimes are required for commercial applications, lifetimes on the order of one nanosecond or more shows promise for optimization of the material (Brant et al., 2017). If the material has strong absorption, one nanosecond leads to approximately 10% conversion efficiency. Research is currently aimed at bismuth compounds like BiI_3 that are thought to be defect tolerant, and characterized by the long lifetimes as a result of this defect tolerance (Brant et al., 2017). Defect tolerant semiconductors have intrinsic point defects that cause slow electron-hole recombination times, and may also have extrinsic or structural defects that contribute to longer lifetimes as well. Yan et al. reports vacancies as energetically favorable, thermodynamically stable, and the most common defects in BiI_3 (2018). Five different types of vacancy defects in monolayer BiI_3 were studied by Yan et al. using first-principle calculations (2018). Results showed that all five defects caused changes in bandgap value but optical absorption stayed consistent. BiI_3 is also reported to have promise as a defect tolerant semiconductor due to its *s*-antibonding in the valence band (Poindexter, 2018).

For this paper, we utilized spectral- and time-resolved photoluminescence spectroscopy to study optical properties of BiI_3 crystals grown by Professor Ronald Grimm and Julia Martin using sublimation in sealed, evacuated ampoules in a two-zone furnace as shown in Figure 3. The source zone was set at 375 °C and the deposition zone was set at 325 °C for six days.

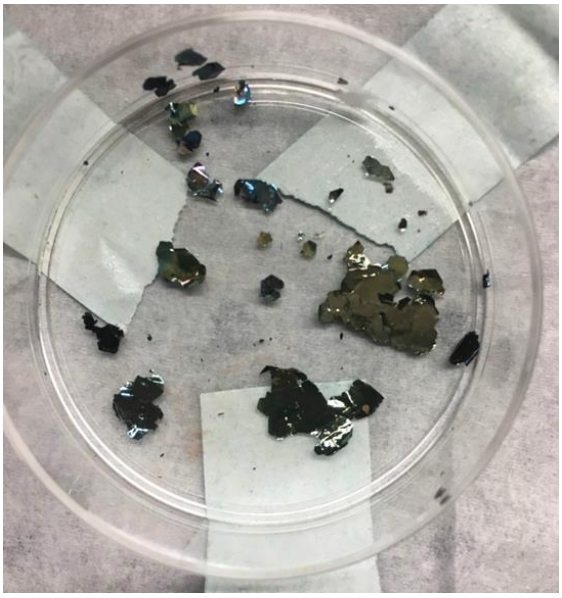

Figure 3: BiI_3 2D flakes

1.4 Photoluminescence Spectroscopy

Photoluminescence spectroscopy is a contact-free, nondestructive probe of the electronic structure of a material. It provides information about the electronic bandgap in semiconductors as well as the energies of various other luminescence electronic states (defects, excitons, etc.) (Ye & Barron, n.d.) As discussed earlier, the process of photoluminescence begins when the energy from an incident photon is absorbed by an electron in the valence band. If this energy is greater than or equal to the bandgap energy, the electron will be excited to the conduction band, leaving a hole in the valence band. Both photoexcited carriers, the electron and the hole, then release

excess kinetic energy by emitting phonons and transferring energy to the crystal lattice. At the conclusion of this process, photoexcited carriers either reach the lowest energy levels in the conduction band (electrons) and valence bands (holes), or the defect-associated trap states. Furthermore, if the exciton binding energy is higher than the thermal energy, which is the case for BiI_3 (Scholtz et al., 2018), excitons may be formed thus further lowering the energy of electrons and holes. The electrons and holes eventually recombine with the electron relaxing back down to the valence band. Energy from the electron-hole pair is then either non-radiatively transferred to the crystal lattice, or released as a luminescence photon. The energy within the emitted light provides information about the energy of the emitting species (free electron-hole pairs, excitons, bound carriers, etc.) (Ye & Barron, n.d., Yu & Cardona, 2010). A diagram of a defect state can be seen below in Figure 4.

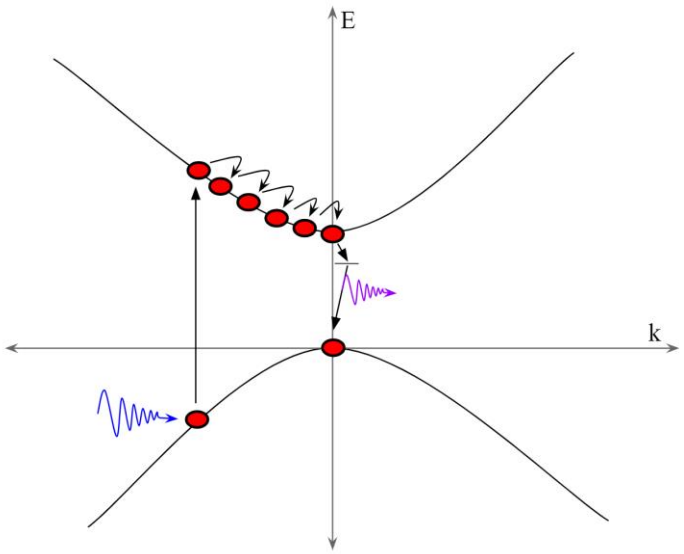

Figure 4: This figure depicts photoluminescence of defect states in which the electron may relax to an energy above the valence band. In this case, if a photon is emitted it will be at a lower energy than the bandgap because it does not make the entire transition at once.

In photoluminescence spectroscopy, the emitted light is collected onto a spectrometer and recorded by detectors to determine the materials energy levels (Fox, 2001). One equation of particular importance to photoluminescence spectroscopy is Equation 1, which shows the relation between wavelength in nanometers and energy in electronvolts of a photon.

$$E = \frac{1239.8}{\lambda} \tag{3}$$

1.5 Time-Resolved Photoluminescence

Typically, time-resolved photoluminescence uses a combination of a pulsed laser and a detector specifically designed to detect single photon events. These two devices must be electronically coupled so that the detector can be synchronized with the pulses of the laser

(Metzger, 2004). A pulsed laser must be used so that there are finite intervals of time during which the sample is excited and emitting. The emission from the sample is then collected by the single photon detector which registers when the photon was detected relative to when the laser pulse was triggered. Over the course of several minutes to several hours photon events are observed and a graph is created displaying the relation between time and intensity of emission. Typical charge carrier lifetimes can be from hundreds of picoseconds to tens of nanoseconds (Kuciauskas, 2013). The level of impurities in the material can impact the carrier lifetime. For example, when silicon is doped with iron particles the carrier lifetime can be adjusted (Ahrenkiel, 2000).

Time correlated single photon counting (TCSPC) is a common method of measuring time-resolved photoluminescence. TCSPC uses a pulsed laser to excite the sample at a constant frequency. The pulsed laser is coordinated with the detector such that when the laser pulse starts the detector starts a timer. The timer counts until a single photon is detected from the emission of the sample, at which point the timer is stopped and the time is recorded. An example of this can be seen below in Figure 5. The time at which the photon arrived is then binned into the appropriate time interval which is directly related to the resolution of the detector. This data is then recorded into a histogram which shows the time decay of the sample (Wahl, 2014). Each data point represents the time difference between the laser pulse and emission so this graph gives us an indication to the radiative lifetime of excitons in the sample (Hoang, 2008).

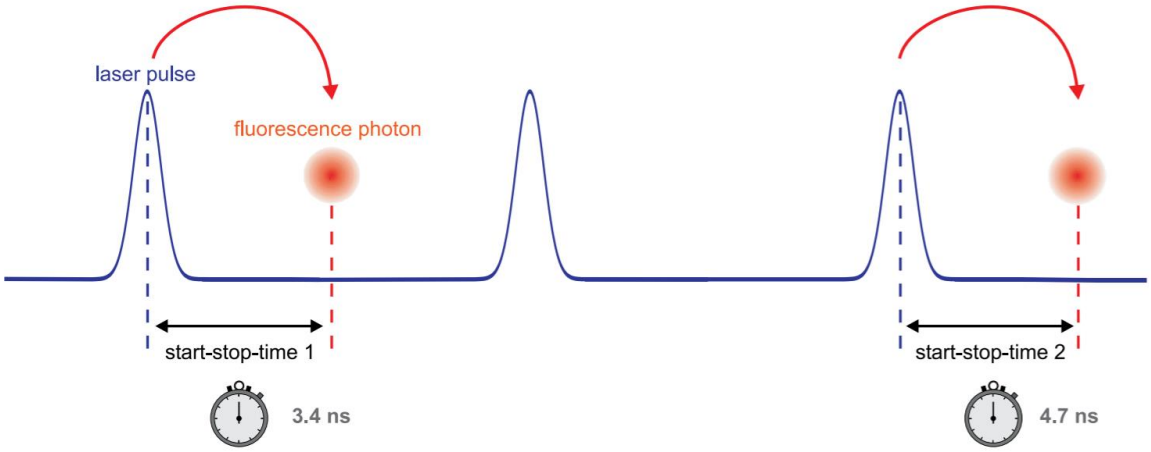

Figure 5: This figure displays an example of multiple laser pulses with recorded photon arrival times. In the event no photon arrives in between two laser pulses no time is recorded (Wahl, 2014).

Chapter 2: Experimental Setup

In this section, we outline the experimental setup used to collect spectrally- and time-resolved photoluminescence spectroscopy data. This includes the laboratory equipment used, the software for data collection and analysis, and the procedure used to measure power dependence.

2.1 Laboratory Equipment Setup

The optical properties of BiI_3 were observed in this paper using photoluminescence spectroscopy. We utilized a Horiba iHR 550 spectrometer and Microscope Optical Spectrometer (MicOS) for spectrally resolved photoluminescence spectroscopy, and coupled this system with a SPD_OEM_VIS and SPD_TCD_mini from Aurea Technology for time-resolved photoluminescence spectroscopy. The SPD_OEM_VIS is a visible spectrum single photon detection module and the SPD_TDC_mini is a time correlation module for single photon detection. Below in Figure 6 a schematic of the MicOS attachment can be seen. Figure 7 shows a diagram of our spectrometer system with our time-resolved devices. A schematic of our Horiba iHR550 can be seen in Figure 8.

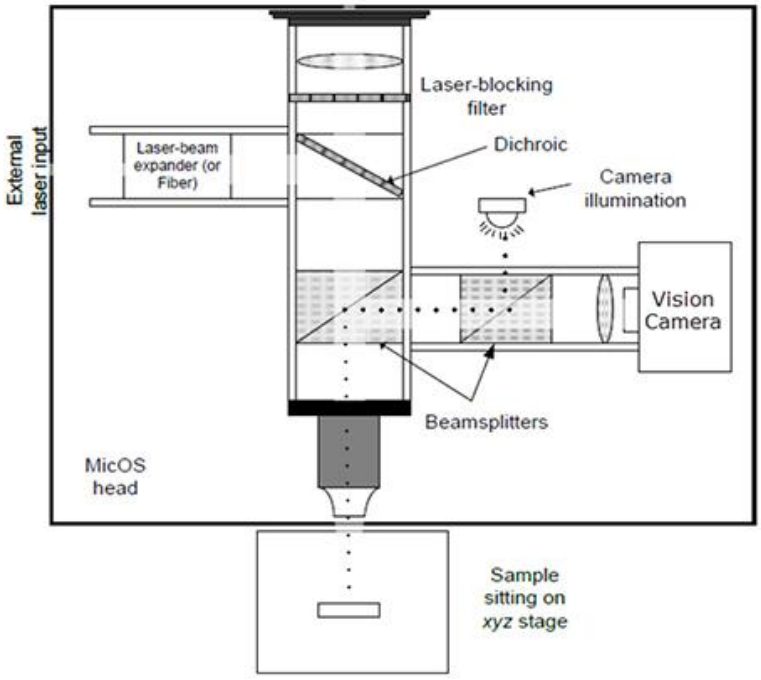

Figure 6: MicOS schematic (Horiba, 2014)

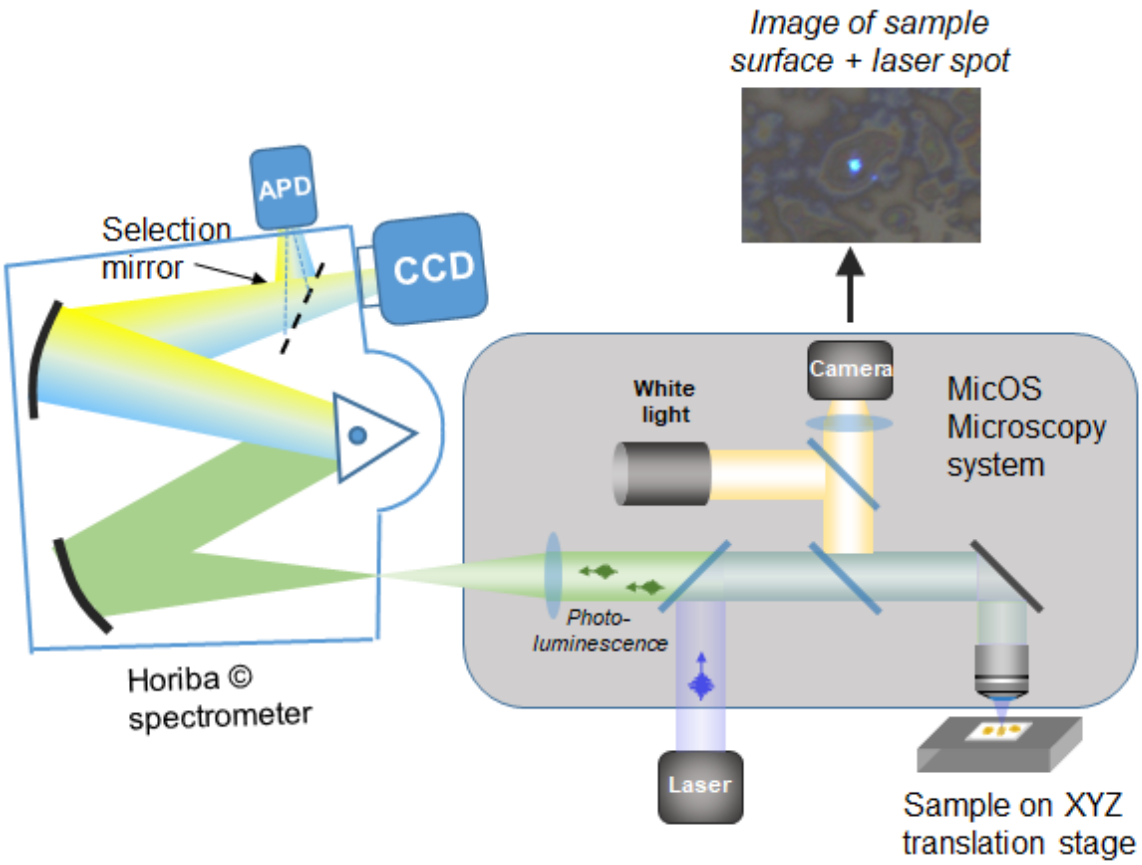

Figure 7: Schematic of our time-resolved and spectrally resolved photoluminescence system including: iHR 550 spectrometer, MicOS attachment, CCD, and fast photodiode.

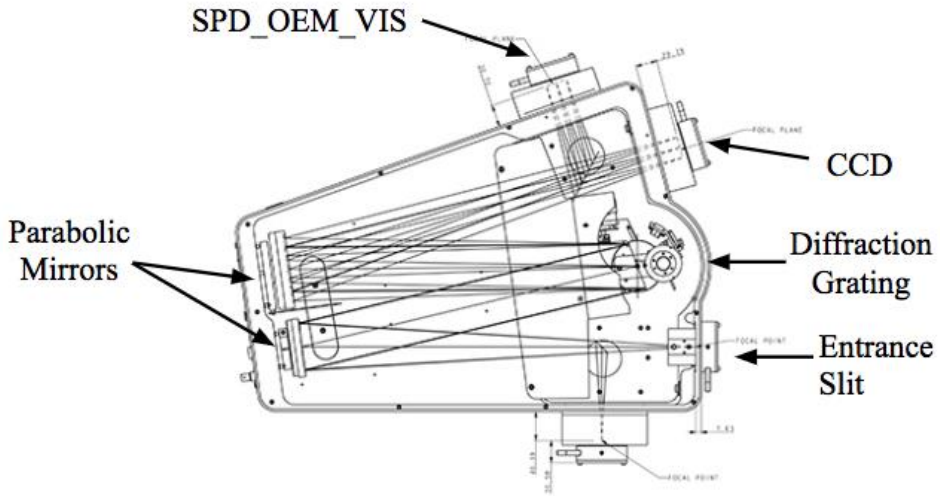

Figure 8: iHR 550 schematic (Horiba, 2013)

A 50x Edmund Optics M Plan Apo NIR parfocal Mitutoyo objective lens was used. This lens has a numerical aperture of 0.26 and focal length of 20 millimeters. The BiI_3 sample was

placed on an xyz stage under the MicOS microscope. The stage is capable of moving vertically up and down to focus on the sample surface and horizontally to move the sample to a desired location. The stage is made up of a flat surface with a circular aluminum sample cup that can be removed or rotated horizontally on the stage surface.

Coupled to the Horiba iHR 550 there is a Synapse CCD detector, also from Horiba. The CCD is able to measure intensity with 1600 by 400 CCD pixels with areas of 16 square micrometers each. To minimize dark current, the CCD is maintained at -60 °C. LabSpec 6.0, a software included with the iHR 550, can be used to change the grating. Diffraction gratings of 150, 600 and 1200 line/mm could be chosen for use. Our paper utilized the 150 line/mm grating. For excitation of the sample, a 485 nm laser was used and a white light was used to focus on the sample with the video feed and for the zeroth order CCD. The 485 nm laser, from Aurea Technology, has options for continuous wave (CW) and pulsed emission.

The laser is coupled into the external input of the MicOS with two mirrors and a periscope (Alignment procedure for the MicOS can be found in Appendix A.) As detailed in Figure 6, a dichroic mirror then reflects the laser off a folding mirror, through the objective and onto the sample. The light emitted from the sample is then detected by passing back up through the objective and off the folding mirror and through the dichroic. The light then passes through a 485 nm filter to block scattered laser light and enters the iHR 550 spectrometer.

Inside the spectrometer the light is reflected off a parabolic mirror and onto a diffraction grating. A diagram of this is displayed in Figure 8 above. As stated before, the diffraction grating can be 150, 600, or 1200 lines/mm, but our paper used 150 lines/mm for measurements. The light is then reflected off another parabolic mirror and either sent to the CCD or the SPD_OEM_VIS. When sent to the CCD, a CCD image or spectra emission graph is presented in LabSpec. When sent to the SPD_OEM_VIS, a time decay histogram is presented in the Aurea Technology software. The alignment procedure of SPD_OEM_VIS can be found in Appendix B.

2.2 LabSpec 6.0, TCSPC Data Acquisition, and Data Analysis

Our experimental setup makes use of two different programs; LabSpec 6.0 and Aurea Technology software. The video feed of the sample on the stage can be viewed in LabSpec and is useful for moving along the sample in the x- and y-directions, as well as focusing the sample and laser spot size vertically. A CCD image is also accessible through LabSpec to ensure the sample is focused or for spatially resolved data. LabSpec can obtain an emission spectra for a range of wavelengths or can display real time data of a specified wavelength. The acquisition time and accumulation of data sets can be adjusted for desired data. In order to obtain time-resolved photoluminescence data, LabSpec must be adjusted so that the real time display is on and set to the peak emission wavelength. Through LabSpec, the Shutter Mode must be set to “always open” and the Exit Mirror to “side,” which directs the emitted light to the SPD_OEM_VIS rather than the CCD. The time-resolved data can then be collected in the Aurea Technology software package. This software is capable of collecting a histogram of the time decay, as well as the raw

data. The data can be adjusted to stop at a specific number of total counts, a maximum number of counts in a specific time bin, or a set amount of time has elapsed.

All data was processed using Origin 2018b data analysis and graphing software. Using the tools available in Origin, we subtracted the background spectra and fit the resulting sample spectra to Gaussian peak functions. Time-resolved photoluminescence data was also analyzed in Origin. The dark count from the time decay histogram (saved from Aurea Technology software) was subtracted and the time decay and system response were plotted on the same axes for comparison. The time decay was then exponentially fit to determine the time constant for radiative lifetime.

2.3 Power Dependence

To measure the dependence of the optical emission on excitation power, we changed the continuous wave (CW) power of the excitation laser in steps of 10%. Excitation spot size was estimated using an ellipse measurement feature in LabSpec, and a ThorLabs power meter model number PM100D was used to record the average incident power on the sample. Excitation power density in W/cm^2 was calculated using those two parameters. To analyze the dependence of the optical emission on the excitation power, each spectrum was fitted to a sum of two Gaussian peaks, and total emission intensity represented by each peak was plotted as a function of the excitation power density.

2.4 Setup Characterization and Validation Using Monolayer MoS_2 and CdSe Quantum Dots

In order to test our experimental setup, we carried out spectrally- and time-resolved measurements on two well-characterized systems, monolayer-thick MoS_2 single nanosheets grown by the group of Professor S. Tongay at Arizona State University and ensembles of CdSe quantum dots purchased from Sigma Aldrich and deposited onto silicon substrate.

Emission energy of CdSe quantum dots is governed by the quantum confinement of the excitons effect and is determined by the average quantum dot diameter (Wong, 2018). Figure 9 below shows an example of the effect of size on emission for CdSe quantum dots. We found that our CdSe quantum dots showed emission at 2.004 electron volts, seen in Figure 10 (a), which is consistent with their average diameter of 6 nm (Donegá, 2006). The spectral and time-resolved measurements can be seen in Figure 10 below. We find that the radiative lifetime of excitons in CdSe sample is 820 ± 80 ps (Prabhu, 1994). In the same graph in Figure 10 (b), we also show instrument response function. It was measured as the apparent decay of the excitation laser scatter with 50-50 beamsplitter in place of the dichroic mirror, and the laser blocking filter removed. We find that we can reliably measure radiative lifetimes >120 ps without the need to deconvolve the system response.

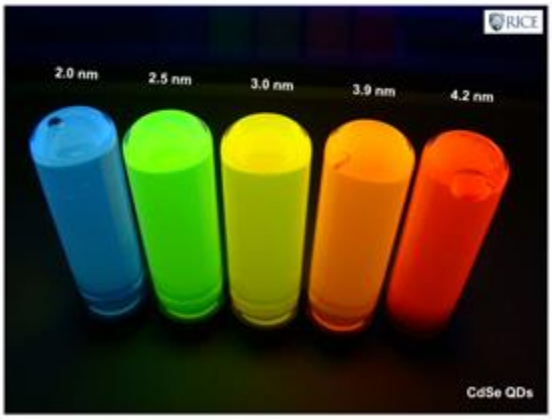

Figure 9: Size confinement effects on emission spectra of CdSe particles (Wong, 2018).

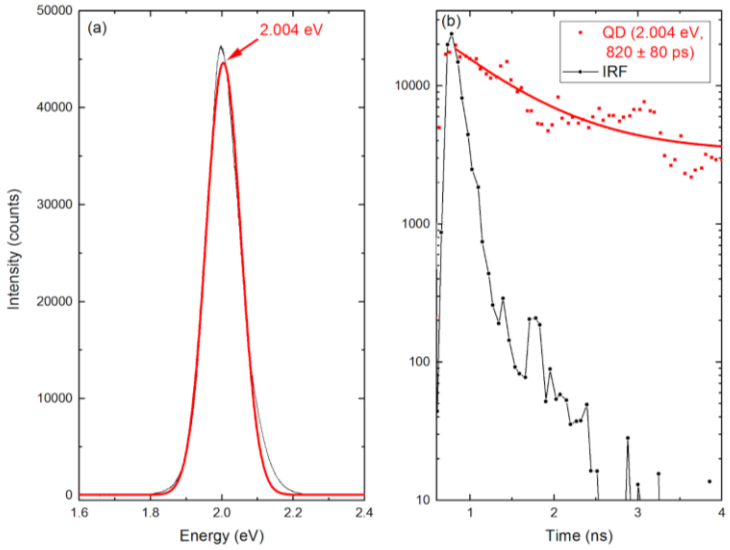

Figure 10: a) Measured emission of CdSe quantum dots b) Measured time-decay of CdSe quantum dots

Another sample we used to verify our ability to measure weak signals from individual 2D material structures was single monolayer-thick nanosheet MoS_2. Like BiI_3, MoS_2 is a 2D material. The individual triangular nanoflakes were fabricated by the group of Professor Tongay in Arizona State University and deposited onto Si substrate. MoS_2 has a direct bandgap, and therefore efficient photoluminescence, in the monolayer limit, and indirect bandgap and weak emission for two or more layers (Kim, 2016). Figure 11 (a) shows that we have observed an emission peak at 1.82 eV, which matches the previously measured value (Fitzgerald, 2018). We also find that the radiative lifetime of MoS_2 is approximately 132 ps (Figure 11 (b)). This value matches estimates for exciton lifetime which is reported to be greater than but approximately equal to 100 ps (Robert, 2016).

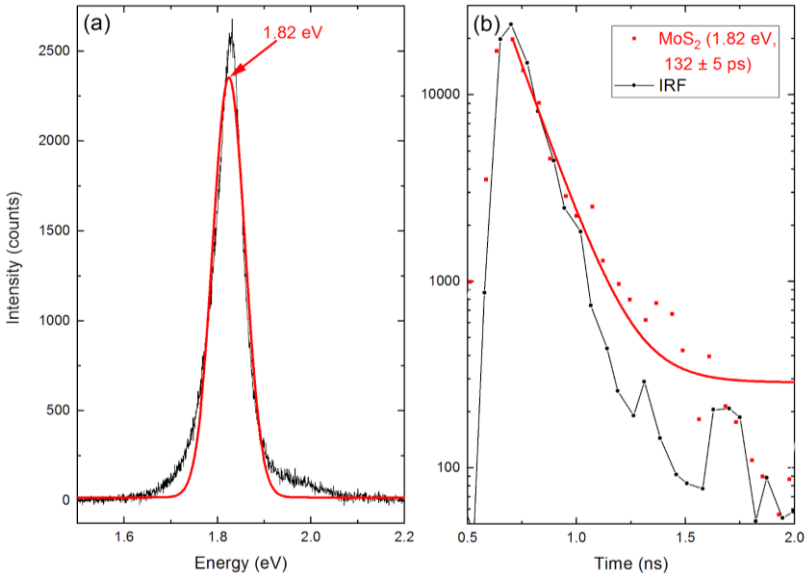

Figure 11: a) Measured emission spectra for MoS_2 b) Measured time-decay for MoS_2

Chapter 3: BiI_3 Photoluminescence

In this section we will outline the results of BiI_3 spectrally- and time-resolved photoluminescence measurements, as well as the dependence of BiI_3 and spectrally-resolved photoluminescence on optical excitation power.

3.1 BiI_3 Results

After establishing our experimental setup and verifying functionality with MoS_2 and CdSe, BiI_3 was studied using spectrally-resolved photoluminescence spectroscopy and time-resolved photoluminescence spectroscopy. Data was taken for ten different locations on the BiI_3 flakes. Pictures of the 10 locations and their corresponding spectra and time-decay graphs can be found in Appendix C. In all studied locations a main peak was found between 1.81-1.83 eV and a wider, weaker shoulder was found at 1.66-1.69 eV. Table 2 summarizes the peak positions and the radiative lifetime of the main peak. The radiative lifetime of the samples was found to be in the range of 240-300 ps. From the sample location pictures and their graphs, we were able to draw that defects did not have an effect on spectral emission or charge carriers. For example, as we can see in Figure 12 (a) the sample has an imperfect surface, whereas in Figure 12 (b) the sample has a homogeneous surface. The graphs for these two locations can be seen in Figure 13 and Figure 14, and the main peak and radiative lifetime are consistent regardless of the two different surface features. Consistent emission peaks and radiative lifetimes are important for materials used in photovoltaic applications because regardless of changes in material structure or surface, the solar cell should have consistent parameters for maximum power output.

Table 2: Emission speaks and lifetimes for all measured spots. Data for spots 3 through 12 can be seen in Appendix C.

Spot number	**Emission energy of Peak 1 (eV)**	**Emission energy of Peak 2 (eV)**	**Emission lifetime of Peak 1 (ps)**	**Description**
1	1.833	1.674	250	Imperfection
2	1.824	1.654	260	Imperfection
3	1.830	1.674	230	Imperfection
4	1.829	1.658	240	Homogeneous
5	1.820	1.690	-	Homogeneous
6	1.823	1.692	270	Imperfection
7	1.810	1.690	280	Imperfection
8	1.830	1.610	130	Imperfection
9	1.828	1.683	210	Terrace
10	1.834	1.677	260	Imperfection on stripes
Average	1.826	1.670	237	-

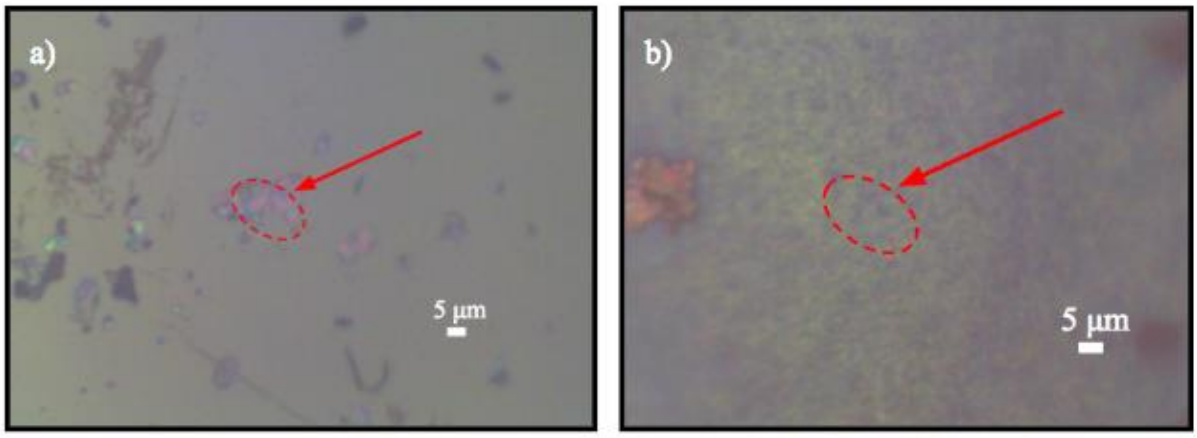

Figure 12: a) Spot 6 on the BiI_3 flake measured on March 20, 2019 b) spot 4 on the BiI_3 flake measured on March 22, 2019

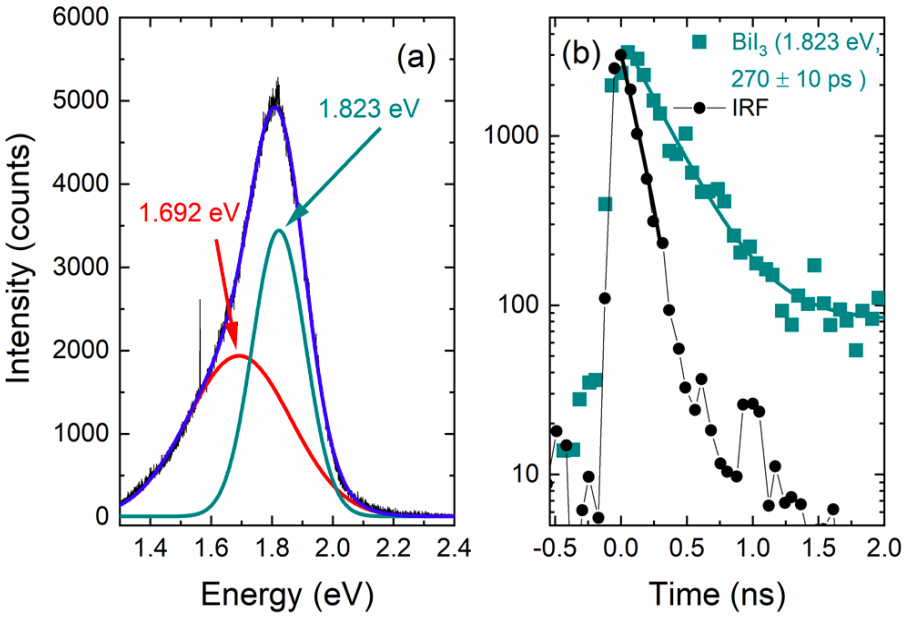

Figure 13: a) Emission spectra and b) Time-decay from spot 6

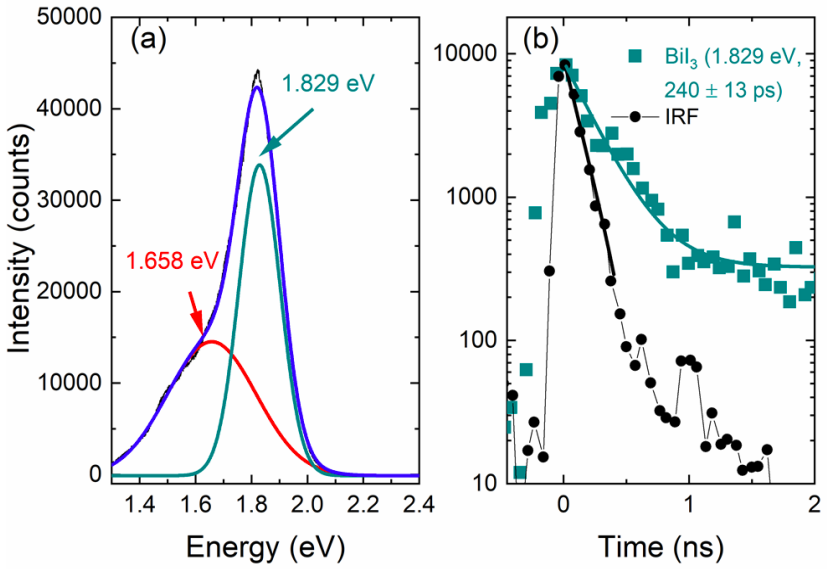

Figure 14: a) Emission spectra and b) Time-decay from spot 4

Based on the literature, we were able to speculate the recombination mechanisms corresponding to the two peaks found in the data. As stated in section 1.3, the indirect bandgap has been found experimentally to be 1.67 eV (Podraza et al., 2013). Therefore, we attribute the wide peak at 1.66-1.69 eV to the indirect bandgap recombination of BiI_3. In a paper published by Scholz and colleagues, the exciton binding energy was found to be between 160-180 meV (2018). When subtracting the exciton binding energy from the direct bandgap of 1.97 eV (stated in section 1.3), the energy emitted from exciton recombination is found and equals

approximately 1.81 eV, which is the same value found for the main peak in the data. Therefore, we attribute the main peak to the recombination of a direct gap exciton. This result confirms prediction of the pronounced excitonic effect in BiI_3 and underscores that they need to be considered when designing BiI_3 solar cells and other devices (Scholz, 2018).

3.2 Power Dependence Results

In addition to spectral and time-resolved data we studied the influence of the excitation power on emission of BiI_3. We measured a set of spectra with different excitation power levels on a homogeneous spot on a BiI_3 flake, which can be seen below in Figure 15. Each spectrum was modeled as a sum of two Gaussian peaks corresponding to the excitonic emission and indirect bandgap emission. Figure 16 plots the dependence of the total emission by those two species as a function of power. For both peaks, we observed some degree of saturation, which is significantly more pronounced for the excitonic peak. We were unable to find a saturation point because at high laser power the sample would start to degrade rapidly at power densities above ~200 W/cm^2. With the data we collected we can see that peak 1, which we believe to be due to exciton recombination, follows a trend which is proportional to $x^{0.68}$. Additionally we found that peak 2, which we believe to be the indirect bandgap emission, is proportional to $x^{0.82}$. These graphs are displayed in Figure 17. Saturation of excitonic emission with increasing excitation power has been reported in other 2D systems and ascribed to exciton-exciton annihilation. Exciton-exciton recombination is a form of non-radiative recombination between two excitons in close proximity which is undesirable for photovoltaic materials (Lee, 2018).

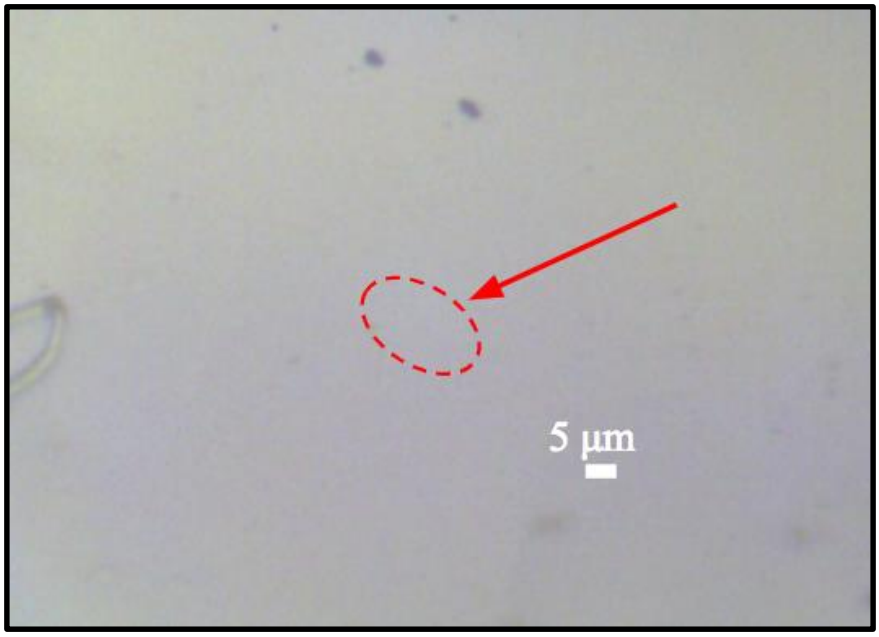

Figure 15: This figure displays the white light image of the location at which we took power dependence measurements. The red dotted outline represents where the laser spot was during measurements.

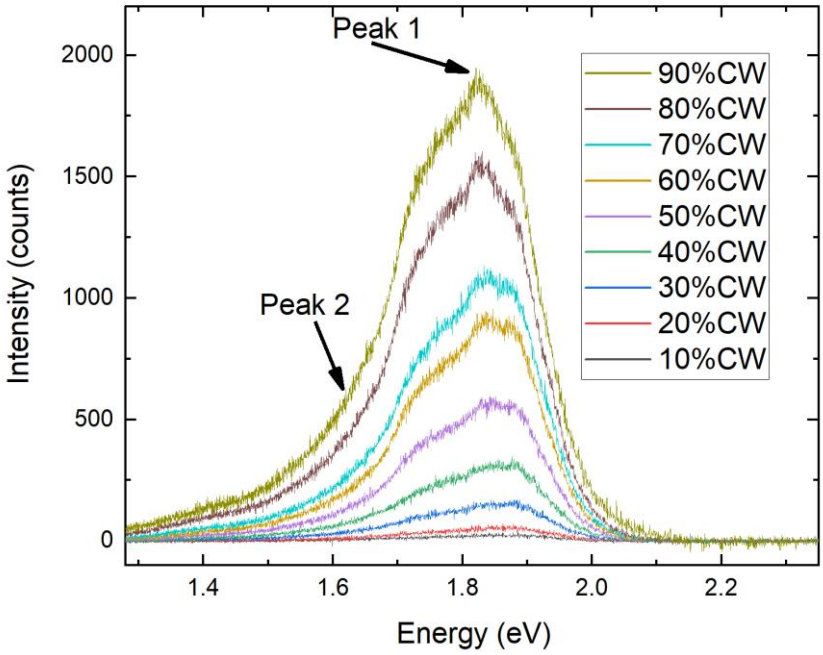

Figure 16: Photoluminescence spectra intensity dependence on CW power percentage ranging from 10% of maximum CW power to 90% CW power.

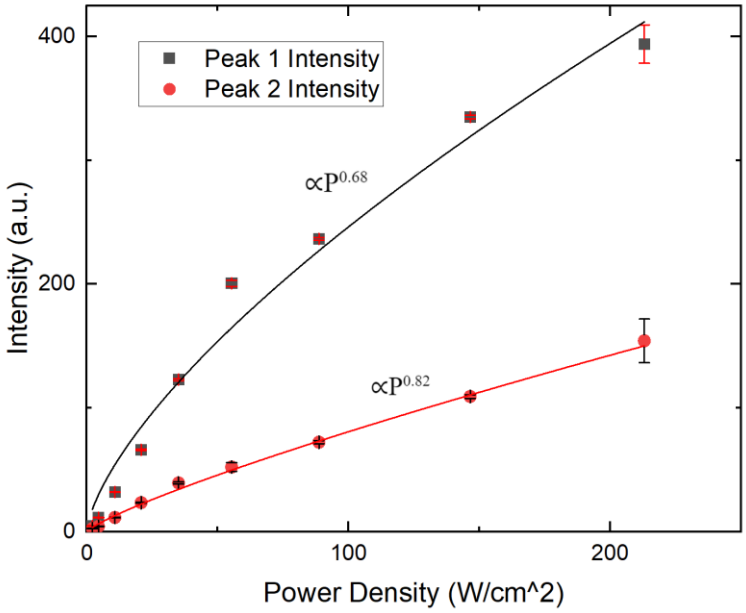

Figure 17: Power density vs emission intensity of BiI_3. Peak 1 (1.82 eV) corresponds to direct bandgap exciton recombination and Peak 2 (1.63 eV) corresponds to the indirect bandgap. The lines are fits of the experimental data to ~P^{α} function, with values of exponent shown in the graph.

Chapter 4: Conclusion and Future Work

We were able to complete the projects goals. We established a working time-resolved photoluminescence spectroscopy apparatus coupled with the already established spectrally-resolved photoluminescence spectroscopy apparatus. We were able to test our experimental setup with two well studied materials, MoS_2 and CdSe, to ensure the system worked properly. We observed the emission spectra and radiative lifetime of BiI_3 through spectrally- and time-resolved photoluminescence spectroscopy on ten different locations on the sample surface. Future research will aim to measure the lifetime of the indirect bandgap emission of BiI_3, as well as correlate this data to THz spectroscopy, which is a measurement that our lab is also capable of doing. Another area of interest will be to look at emission intensity decay and emission intensity variation of BiI_3 samples. During data collection we noted that the emission intensity of a location on the BiI_3 samples decreased over a period of time but were unable to explore this finding further. The emission intensity also changed from location to location on the BiI_3 samples. The peaks remained constant but their intensity counts varied. Research into why this variation occurs could reveal important information about BiI_3 and its material properties. Additionally, after the BiI_3 samples had been exposed to air and light for a period of time, the emission intensity varied. The two peaks were still present, but the intensity counts correlated to the peaks had changed. Future efforts should focus on the effects of oxidation on BiI_3 photoluminescence spectroscopy.

References

Ahrenkiel, R, et al. “Injection Level Lifetime Spectroscopy of Impurities in Semiconductors.” *Taylor and Francis Online*, 2000, www.tandfonline.com/doi/pdf/10.1179/026708400322911537?needAccess=true.

Aurea Technology. 2018. “SPD_OEM_VIS Alignment Procedure.” Operation Manual. Nov.

Brant, R.E., Kurchin, R.C., Hoye, R.L.Z., Poindexter, J.R., Wilson, M.W.B., Sulekar, S., Lenahan, F., Yen, P.X.T., Stevanovic, V., Nino, J.C., Bawendi, M.G., & Buonassisi, T. (2015). Investigation of Bismuth Triiodide (BiI_3) for Photovoltaic Applications. *Journal of Physical Chemistry Letters, 6*, 4297-4302. doi: http://dx.doi.org/10.1021/acs.jpclett.5b02022

Brandt, R.E., Poindexter, J.R., Gorai, R., Kurchin, R.C., Hoye, R.L.Z., Nienhaus, L., Wilson, M.W.B., Polizzotti, J.A., Sereika, R., Zaltauskas, R., Lee, L.C., MacManus-Driscoll, J.L., Bawendi, M., Stevanovic, V., & Buonassisi, T. (2017). Searching for “Defect-Tolerant” Photovoltaic Materials: Combined Theoretical and Experimental Screening. *Chem. Mater. 29*, 4467-4674. doi: http://dx.doi.org/10.1021/acs.chemmater.6b05496

Callister, W. D. (2014). *Materials Science and Engineering: An Introduction*. Hoboken: Wiley.

Castellanos-Gomez, A. (2016). Why all the fuss about 2D semiconductors? *Nature Photonics, 10*. doi: http://www.nature.com/naturephotonics

Donegá, C. De Mello, et al. “Size- and Temperature-Dependence of Exciton Lifetimes in CdSe Quantum Dots.” *Physical Review B*, vol. 74, no. 8, 2006, doi:10.1103/physrevb.74.085320.

Dvorak, M., Wei, S., & Wu, Z. (2013). Origin of the Variation of Exciton Binding Energy in Semiconductors. *Physical Review Letters, 110*(1). doi: http://dx.doi.org/10.1103/PhysRevLett.110.016402

Edvinsson, T. (2018). Optical quantum confinement and photocatalytic properties in two-, one- and zero-dimensional nanostructures. *Royal Society Open Science, 5*. Doi: http://dx.doi.org/10.1098/rsos.180387

Fitzgerald, Patrick D. (2018). *Spatially Resolved Photoluminescence Spectroscopy of 2D Nanomaterials* (Undergraduate Major Qualifying Project No. E-project-042618-142118) Retrieved from Worcester Polytechnic Institute Electronic Projects Collection: https://web.wpi.edu/Pubs/E-project/Available/E-project-042618-142118/

Fox, Mark (2001). *Optical Properties of Solids.* Oxford, England: Oxford University Press.

Ghoshal, Sib Krishna (n.d.). *SSCP 4473: Spectroscopy & Materials Analysis, Chapter 6 notes* [PowerPoint Slides]. Retrieved from http://ocw.utm.my/file.php/351/ocw-chapter-6.pdf

Gupta, Ankur., Sakthivel, Tamilselvan, & Seal, Sudipta (2015). Recent development in 2D materials beyond graphene. *Progress in Materials Science, 73,* 44-126. https://doi.org/10.1016/j.pmatsci.2015.02.00

Hamdeh, U.H., Nelson, R.D., Ryan, B.J., Bhattacharjee, U., Petrich, J.W., & Panthani, M.G. (2016). Solution-Processed BiI_3 Thin Films for Photovoltaic Applications: Improved Carrier Collection via Solvent Annealing. *Chemistry of Materials, 28,* 6567-6574. doi: http://dx.doi.org/10.1021/acs.chemmater.6b02347

Hoang, T. (2008). *Investigation of Single Semiconductor Nanowire Heterostructures Using Polarized Imaging Spectroscopy* (PhD thesis). University of Cincinnati, Cincinnati, Ohio, United States of America.

Horiba. 2013. "iHR Fully Automated Imaging Spectrometer." Operation Manual. 28 Feb.

Horiba. 2014. “MicOS Microscope Optical Spectrometer.” Operation Manual. 21 Mar.

Hsueh, H., Li, J., Ho, C. (2018). Polarization Photoelectric Conversion in Layered GeS. *Advanced Optical Materials, 6*(4). doi: https://doi-org.ezproxy.wpi.edu/10.1002/adom.201701194

Introduction to Semiconductors. (2009, November 23). Retrieved from https://warwick.ac.uk/fac/sci/physics/current/postgraduate/regs/mpagswarwick/ex5/intro/

Jenkins, Tudor (2005). A brief history of… semiconductors. *Physics Education, 40(5),* (430-439). https://doi-org.ezproxy.wpi.edu/10.1088/0031-9120/40/5/002

Kim, Jung Gon, et al. “Effect of Interlayer Interactions on Exciton Luminescence in Atomic-Layered MoS_2 Crystals.” *Nature News*, Nature Publishing Group, 15 July 2016, www.nature.com/articles/srep29813.

Kuciauskas, Darius, et al. “Minority Carrier Lifetime Analysis in the Bulk of Thin-Film Absorbers Using Subbandgap (Two-Photon) Excitation.” *Minority Carrier Lifetime Analysis in the Bulk of Thin-Film Absorbers Using Subbandgap (Two-Photon) Excitation - IEEE Journals & Magazine*, 2013, ieeexplore.ieee.org/stamp/stamp.jsp?tp=&arnumber=6553424.

Lee, Yongjun, et al. “Impeding Exciton–Exciton Annihilation in Monolayer WS2 by Laser Irradiation.” *ACS Photonics*, vol. 5, no. 7, 2018, pp. 2904–2911., doi:10.1021/acsphotonics.8b00249.

Metzger, W, et al. *Time-Resolved Photoluminescence and Photovoltaics* . National Renewable Energy Laboratory, Dec. 2004, www.nrel.gov/docs/fy05osti/37028.pdf.

Peiponen, K., Zeitler, A., & Kuwata-Gonokami, 2013. *Terahertz Spectroscopy and Imaging*. Berlin, Heidelberg: Springer. doi: https://doi.org/10.1007/978-3-642-29564-5

Podraza, N., Qui, W., Hinojosa, B., Xu, H., Motyka, M., Phillpot, S., Baciak, J., Trolier-McKinstry, S., & Nino, J. (2013). Band gap and structure of single crystal BiI_3: Resolving discrepancies in literature. *Journal of Applied Physics, 114*. doi: https://doi.org/10.1063/1.4813486

Poindexter, J. (2018). *Defects and charge-carrier lifetime in early-stage photovoltaic materials: relating experiment to theory* (PhD thesis). Massachusetts Institute of Technology, Massachusetts, United States of America.

Poole, Ian. "Semiconductor Materials Types List." *Op Amp Gain | Operational Amplifier Calculation Equations | Radio-Electronics.com*, www.radio-electronics.com/info/data/semicond/semiconductor/semiconductor-materials-types-list.php

Prabhu, S. S., et al. "Picosecond Radiative Decay of Free and Bound Excitons and Excitonic Molecules in CdSe." *Physical Review B*, vol. 50, no. 24, 1994, pp. 18098–18105., doi:10.1103/physrevb.50.18098.

Rao, P. (2019). *Introduction to Nanomaterials and Nanotechnology* [PowerPoint presentation] Retrieved from WPI Canvas.

Robert, C., et al. "Exciton Radiative Lifetime in Transition Metal Dichalcogenide Monolayers." *Physical Review B*, vol. 93, no. 20, 2016, p. 5., doi:10.1103/physrevb.93.205423.

Roduner, E. (2006). Size matters: why nanomaterials are different. *Chemical Society Reviews, 35*, 583-592. doi: 10.1039/b502142c

Scholz, M., Oum, K., & Lenzer, T. (2018). Pronounced exciton and coherent phonon dynamics in BiI_3. *Phys. Chem. Chem. Phys., 20*, 10677-10685. doi: 10.1039/c7cp07729g

Seeger, K (1999). *Semiconductor Physics*. Berlin, Heidelberg: Springer. doi: https://doi-org.ezproxy.wpi.edu/10.1007/978-3-662-03797-3

Shen, C., & Wang, G. (2017). The effects of stacking patterns and interlayer coupling on electronic and optical properties of bilayer BiI_3. *Journal of Materials Science, 52*(19). doi: 10.1007/s10853-017-1325-x

Smith, Andrew M., and Shuming Nie. "Semiconductor Nanocrystals: Structure, Properties, and Band Gap Engineering." *Accounts of Chemical Research*, vol. 43, no. 2, 2010, pp. 190–200., doi:10.1021/ar9001069.

Sze, S. M. (2007). *Physics of Semiconductor Devices*. Hoboken, New Jersey: Wiley-Interscience.

Tiwari, D., Alibhai, D., & Fermin, D.J. (2018). Above 600 mV Open-Circuit Voltage BiI_3 Solar Cells. *ACS Energy Letters, 3*, 1882-1886. doi: 10.1021/acsenergylett.8b01182

Wahl, Michael. "Time-Correlated Single Photon Counting." PicoQuant GmbH. 2014.

Wei, Q., Chen, J., Ding, P., Shen, B., Yin, J., Xu, F., Xia, Y., & Liu, Z. (2018). Synthesis of Easily Transferred 2D Layered BiI_3 Nanoplates for Flexible Visible-Light Photodetectors. *Applied Materials & Interfaces, 10*, 21527-21533. doi: 10.1021/acsami.8b02582

Wong, Michael. "Quantum Dots: The Basics." *FindLight Blog*, Rice University, 2 Aug. 2018, www.findlight.net/blog/2018/08/02/quantum-dots-basics/.

Xia, F., Wang, H., Xiao, D., Dubey, M., & Ramasubramaniam, A. (2014). Two-dimensional material nanophotonics. *Nature Photonics, 8*. doi: http://www.nature.com/doifinder/10.1038/nphoton.2014.271

Xu, M., Liang, T., Shi, M., & Chen, H. (2013). Graphene-Like Two-Dimensional Materials. *Chemical Reviews, 113*, 3766-3789. doi: http://dx.doi.org/10.1021/cr300263a

Yan, H., Ziyu, H., Xu, G., Xiaohong, S. (2018). Structural, electronic and photocatalytic properties of atomic defective BiI_3 monolayers. *Chemical Physics Letters, 691*, 341-346. doi:https://doi.org/10.1016/j.cplett.2017.11.044

Ye, R., & Barron, A. R. (n.d.). Photoluminescence Spectroscopy and its Applications. Retrieved From https://cnx.org/contents/gbsDEZju@2/Photoluminescence-Spectroscopy-and-its - Applications

Yu, Peter Y., & Cardona, Manuel (2010). *Fundamentals of Semiconductors: Physics and Materials Properties*. Heidelberg: Springer.

Zhang, Q., Uchaker, E., Candelaria, S., & Cao, G. (2013). Nanomaterials for energy conversion and storage. *Chem. Soc. Rev., 42*, 3127. doi: 10.1039/c3cs00009e

Appendix A: MicOS Alignment

Before components inside the MicOS head are adjusted for alignment, the excitation laser was turned on and the alignment was checked at all points along the beam path before the beam entered the external input of the MicOS head (Figure 18). If alignment then was still not satisfactory, the screws on the plastic covering of the MicOS were loosened and the plastic cover was removed. With the mirror target screwed into the alignment tube, we screwed the alignment tube into the side of the dichroic mirror, where the laser beam enters through the external input. Checking the alignment here, the laser beam should enter the alignment tube and return along the same path. If the returning laser beam was off center, the mirrors or periscope coupling the laser to the MicOS needed to be adjusted.

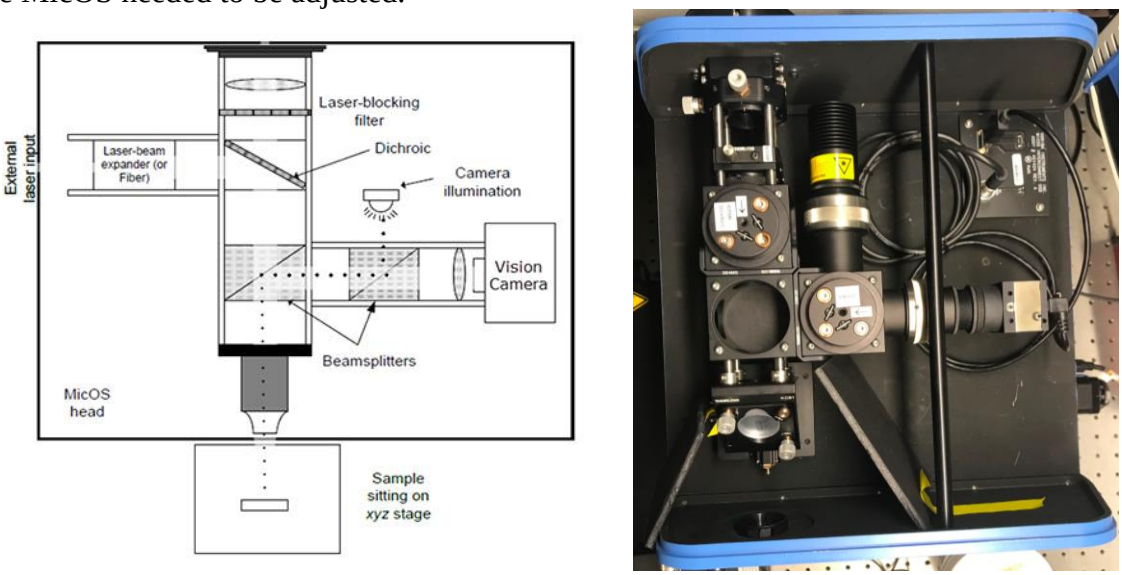

Figure 18: MicOS schematic and picture inside MicOS head

Next, the alignment of the dichroic mirror was checked. The folding mirror mount was removed from the system, and the black cap was removed from the MicOS head by squeezing from the inside. The alignment tube with the frosted-glass target screwed into it was then placed through the hole where the black cap was, and screwed into the front facing cube. Using the rotation and tilt adjustments on top of the dichroic mount, the dichroic was rotated until the laser beam was centered on the alignment target. Ideally, this will be at 45 degrees to the normal of the incoming laser beam, so that the laser beam travels away from the spectrometer. To secure the alignment of the dichroic, two of the four screws on the dichroic mount were tightened to lock the position. The alignment target was then removed and the folding mirror was put back into place.

The folding mirror was then the next component to be adjusted. To start, the alignment tube with the frosted-glass target still in place, was screwed into the opening on the underside of the MicOS. To see alignment on the frosted-glass target, a front-facing phone camera or mirror was placed underneath the target. The tilt controls on the folding mirror were used to center the beam on the frosted-glass target. When the alignment here was sufficient, the frosted-glass target was replaced by the mirror target, with the alignment tube still screwed into the underneath of the MicOS. The bullseye target was placed on the entrance of the spectrometer because the mirror target will reflect the laser beam back up and into the spectrometer. The tilt controls on

the folding mirror were used here again to position the laser beam on the center of the bullseye target. This can be further optimized by using the image of the beam captured by the CCD on the spectrometer and using the folding mirror tilt controls to adjust.

If the vision system of the MicOS system did not need alignment, all targets could be removed. Alignment of the vision system will help to illuminate light from the LED to the sample and directing the reflected light back to the camera. To start, the LED white light was turned on using the LED controller. A course alignment was first done by eye. To center the LED light on the target, the rotation and tilt controls on beamsplitter 1 were used (Figure 18). With the excitation laser on, the tilt and rotation controls on beamsplitter 2 (Figure 18) were used to align the image of the laser with the center of the LED beam. With the vision camera turned on in LabSpec, the alignment tube with mirror target was screwed back into the underside of the MicOS, and the controls of beamsplitter 2 were adjusted to center the image of the laser on the vision camera. The laser power should be lowered here to increase the accuracy. Removing the alignment tube and placing the microscope objective into the object mount, the laser dichroic was adjusted slightly so that the laser beam diameter changes in size but remains circular as the stage is lowered and raised. This ensured the beam is centered on the objective's axis.

Appendix B: SPD_OEM_VIS Alignment

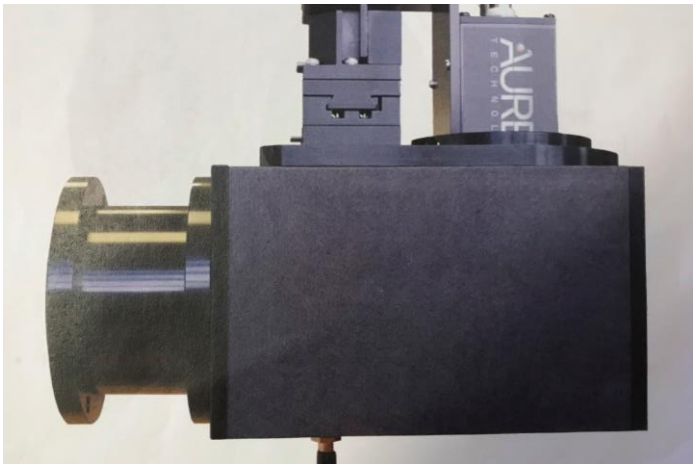

Figure 19: Aurea Technology SPD_OEM_VIS (Aurea Technology, 2018)

To measure accurate and reliable time-decay photoluminescence, the Aurea Technology SPD_OEM_VIS (Figure 19) coupled to the iHR550 spectrometer was re-aligned periodically. Alignment occured anytime the "Stop rate (Hz)" value was low. The "Stop rate (Hz)" value was found in the upper right hand corner of the Aurea Technology software (Figure 20). Through alignment, this value was maximized and allowed for more reliable time-decay photoluminescence data to be collected.

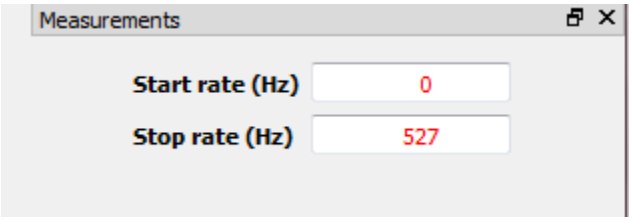

Figure 20: "Stop rate (Hz)" (Aurea Technology, 2018)

To align the SPD_OEM_VIS, three screws were adjusted to position the detector properly with the optical signal. There is an x-, y-, and z-axis screw to allow adjustment of the SPD_OEM_VIS in all three directions, as seen in Figure 21. The x- and y-axis screws were adjusted using a "2" hexagonal key and the z-axis screw was adjusted using a "3" key. The Aurea Technology alignment procedure recommends adjustment of the x- and y-axis first, followed by the z-axis (Aurea Technology, 2018). The screws were adjusted iteratively until the "Stop rate (Hz)" was maximized.

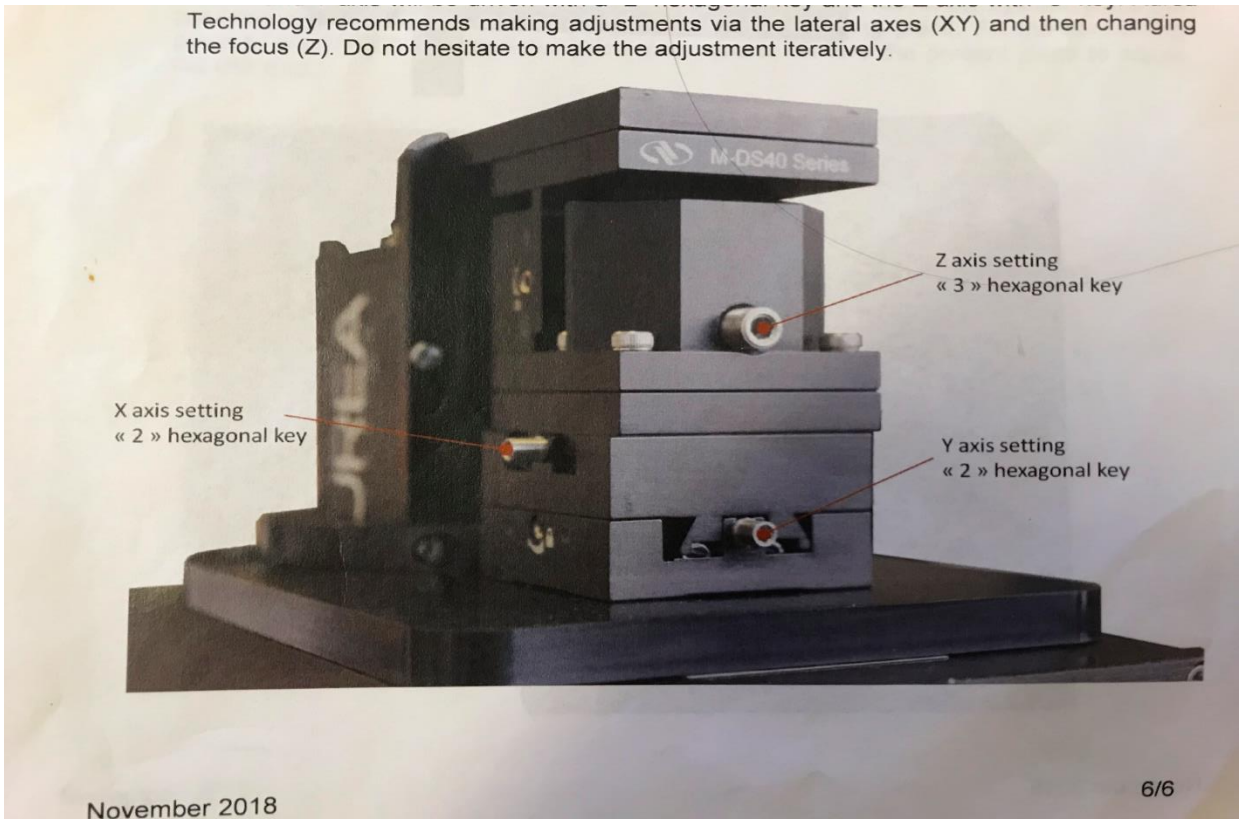

Figure 21: X-, Y-, Z-axis screws for adjustments (Aurea Technology, 2018)

Appendix C: BiI_3 Data

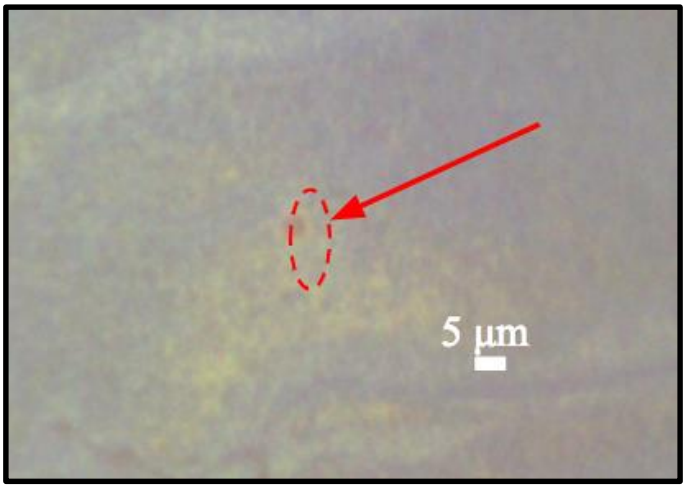

Figure 22: Spot 1 on the BiI_3 flake measured on March 20, 2019

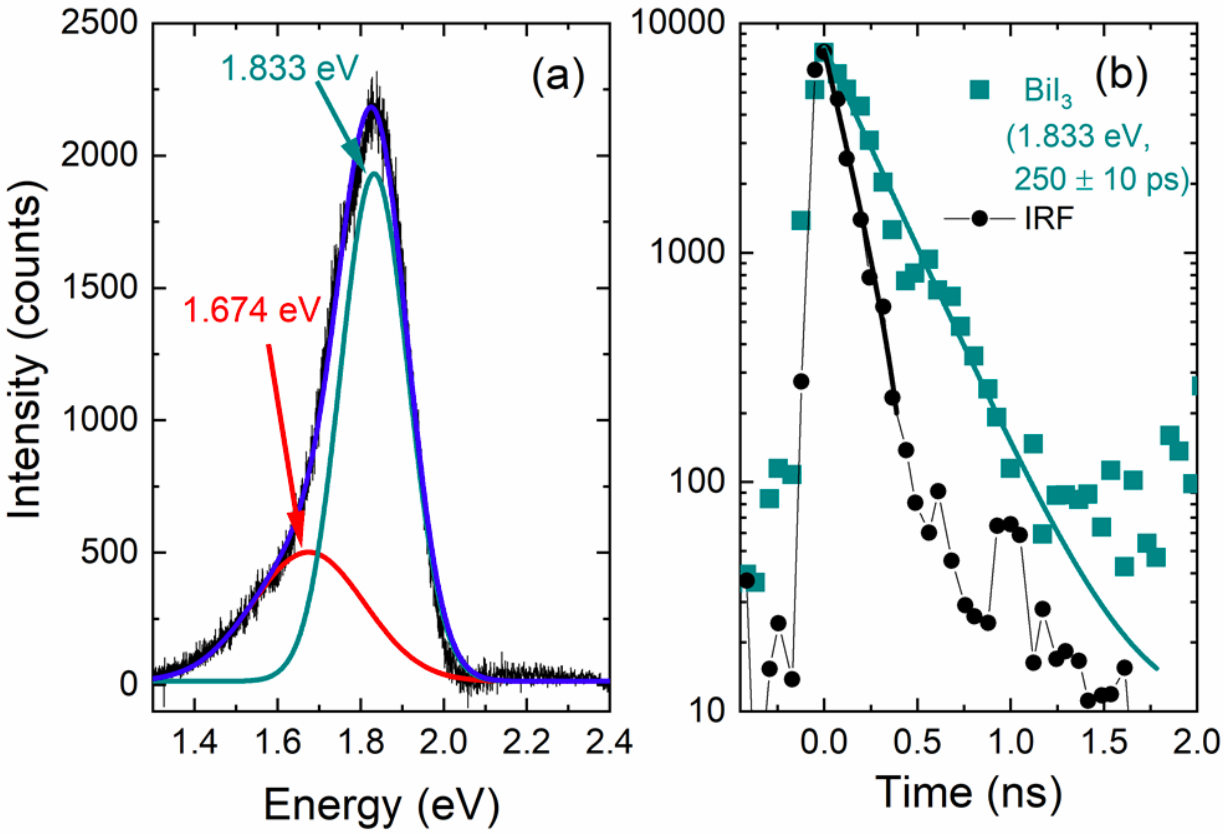

Figure 23: a) Spectra and b) time-decay from spot 1 displayed in Figure 22

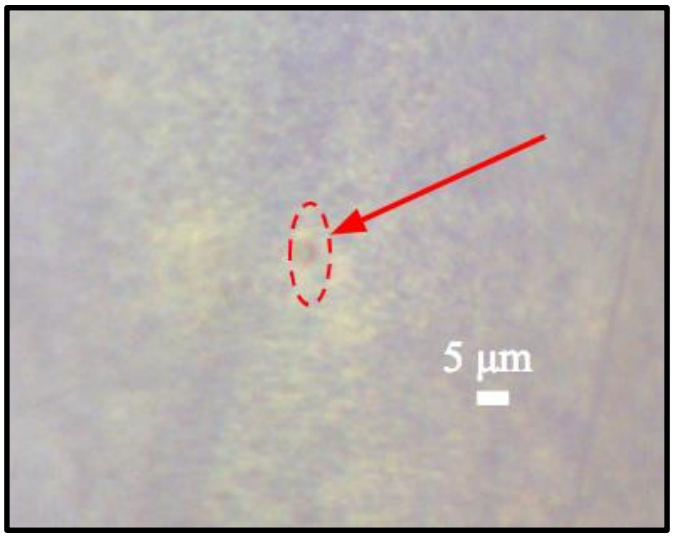

Figure 24: Spot 2 on the BiI_3 flake measured on March 20, 2019

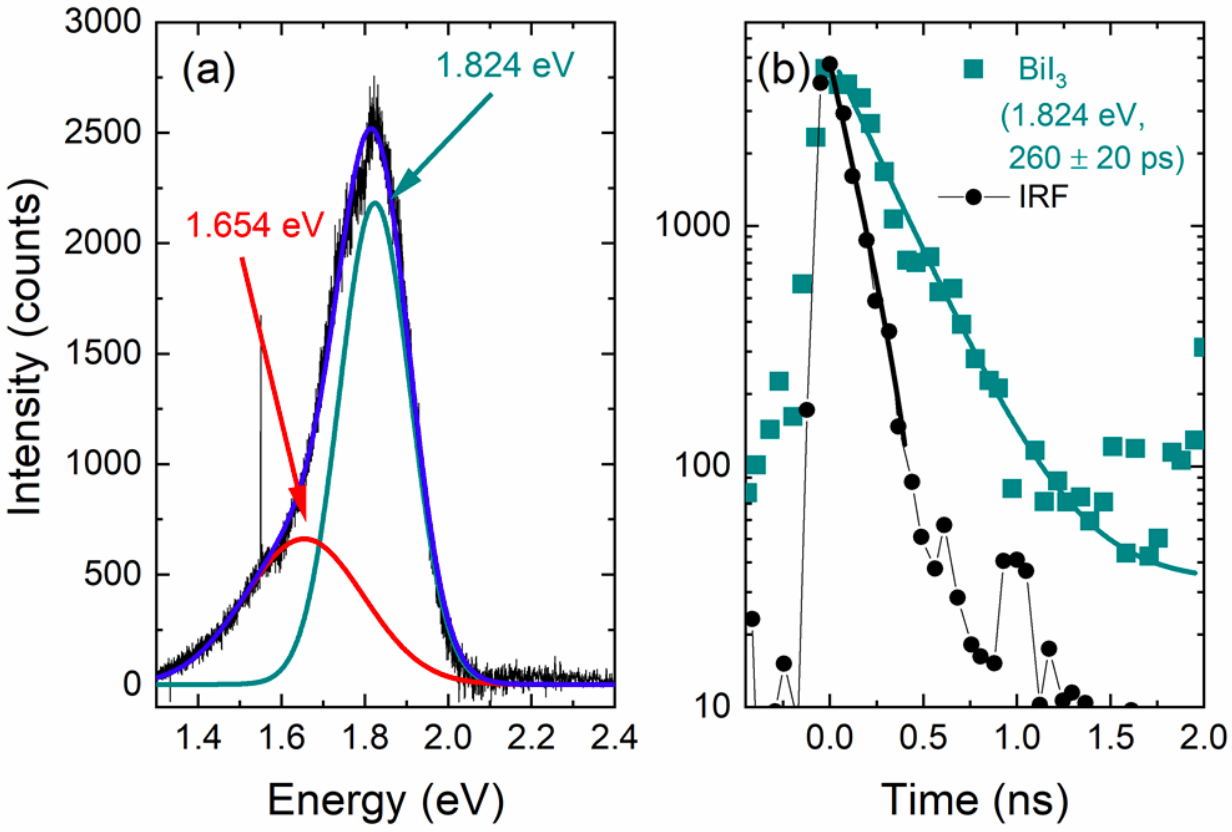

Figure 25: a) Spectra and b) time-decay from spot 2 displayed in Figure 24

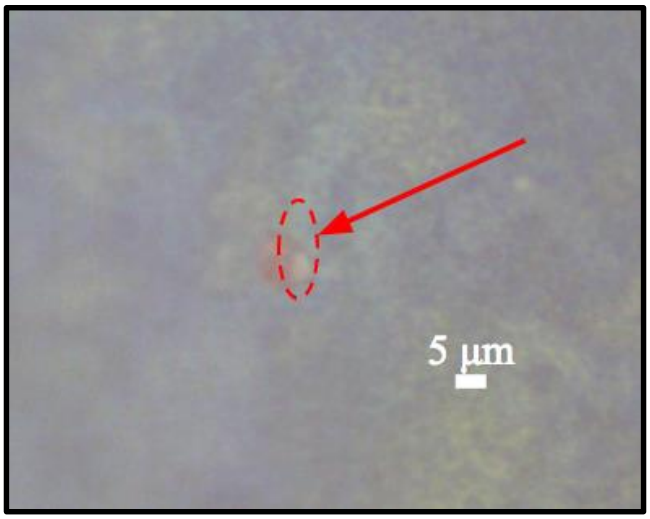

Figure 26: Spot 3 on the BiI_3 flake measured on March 20, 2019

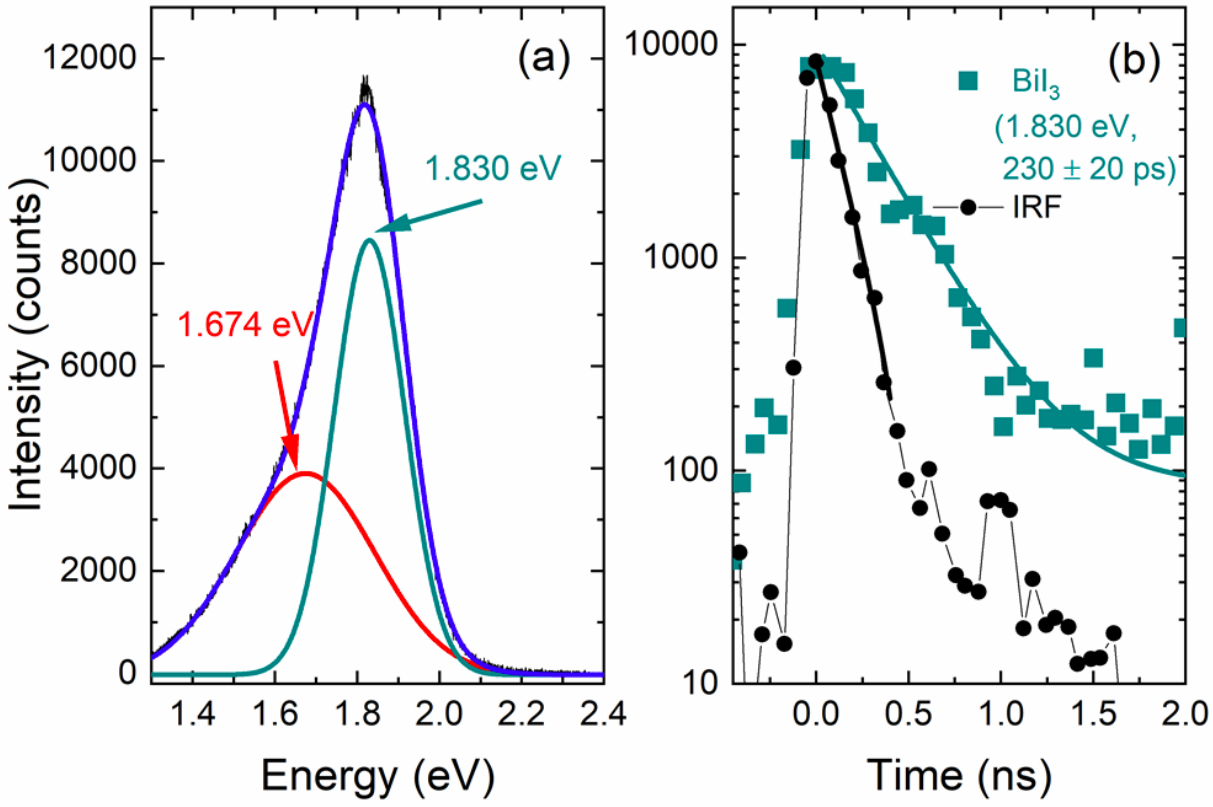

Figure 27: a) Spectra and b) time-decay from spot 3 displayed in Figure 26

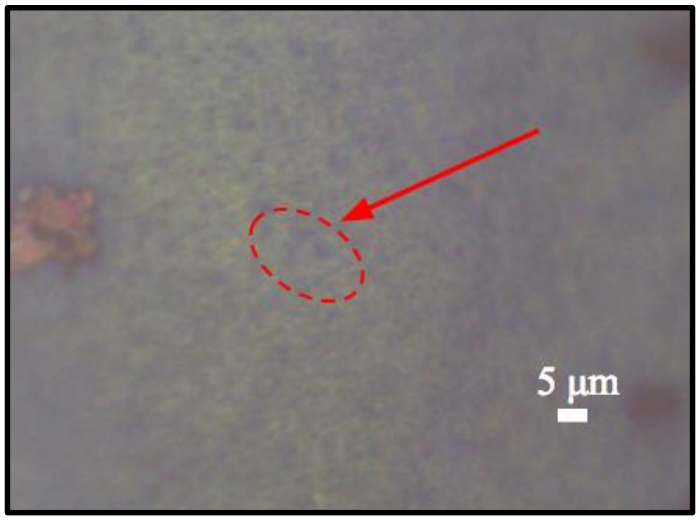

Figure 28: Spot 4 on the BiI_3 flake measured on March 20, 2019

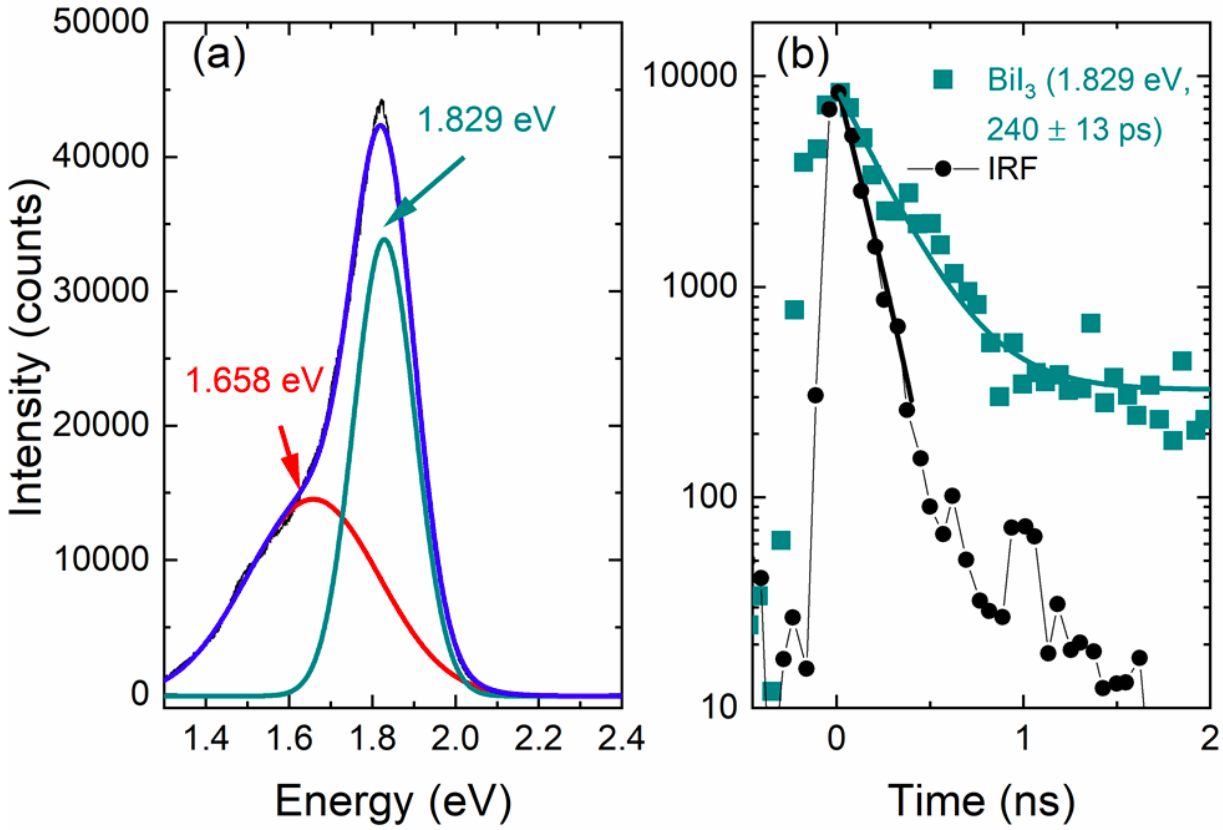

Figure 29: a) Spectra and b) time-decay from spot 4 displayed in Figure 28

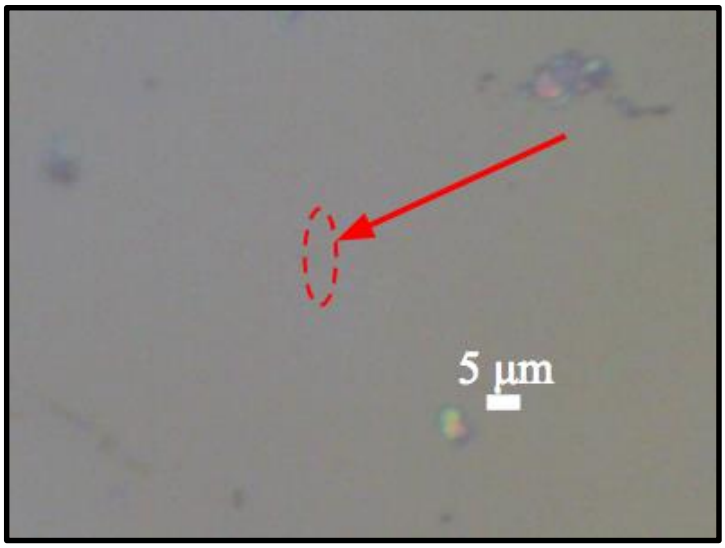

Figure 30: Spot 5 on the BiI_3 flake measured on March 22, 2019

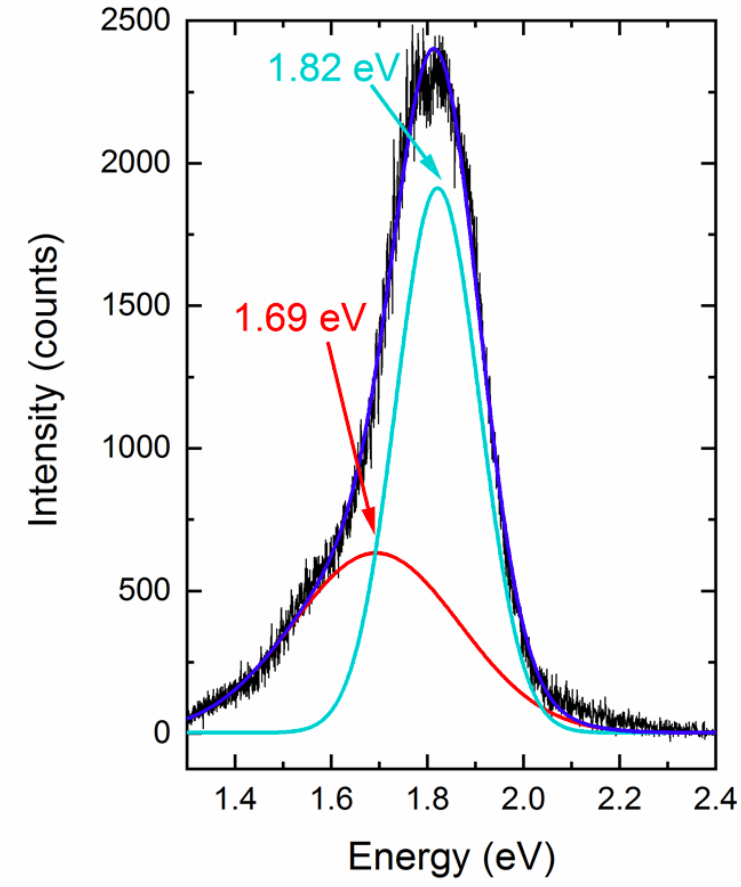

Figure 31: a) Spectra from spot 5 displayed in Figure 30

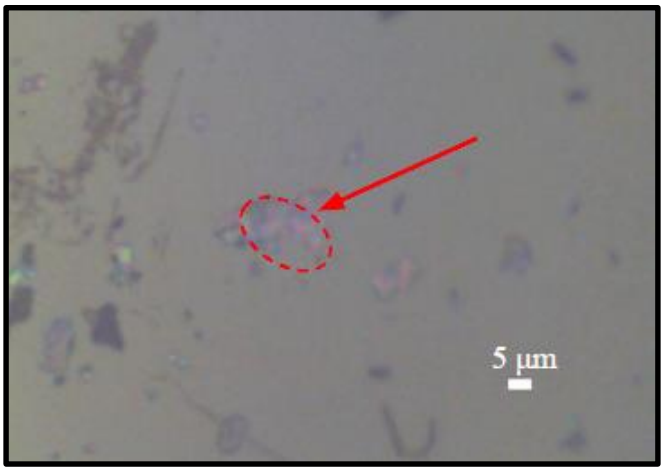

Figure 32: Spot 6 on the BiI_3 flake measured on March 22, 2019

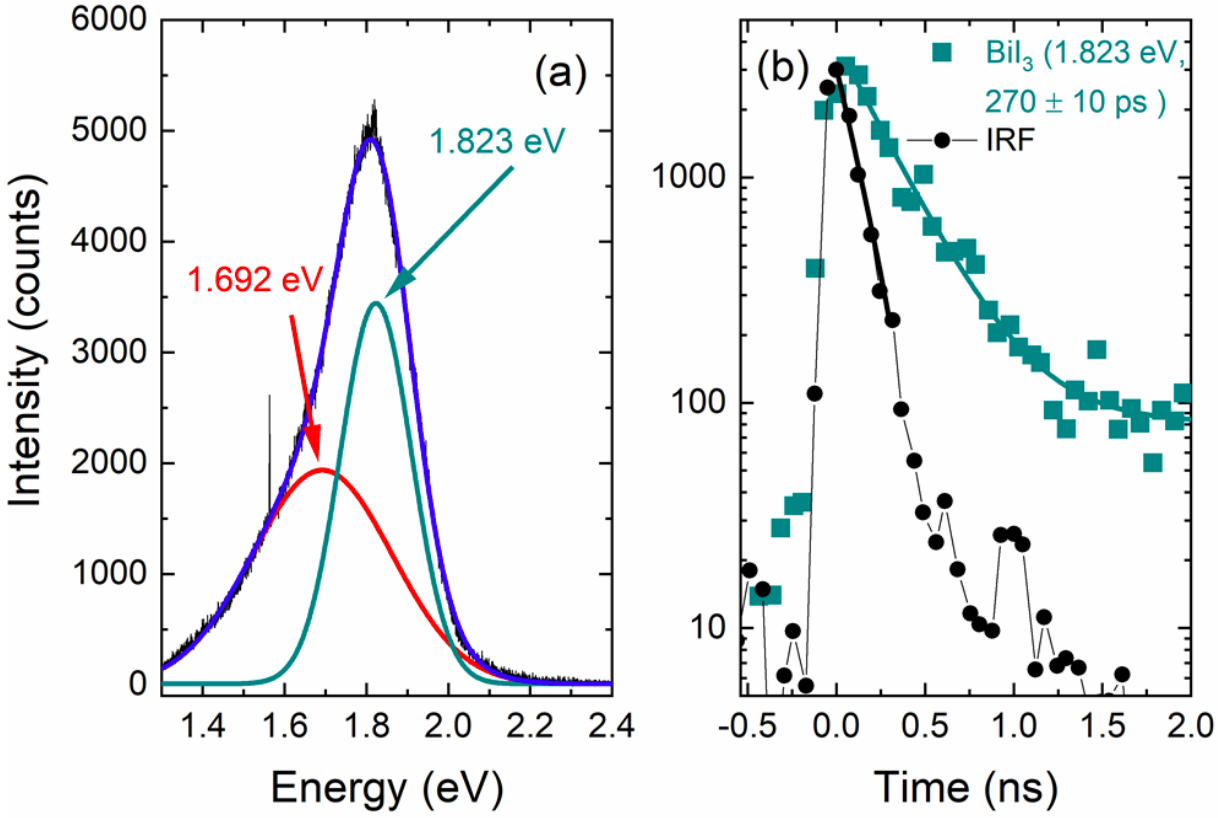

Figure 33: a) Spectra and b) time-decay from spot 6 displayed in Figure 32

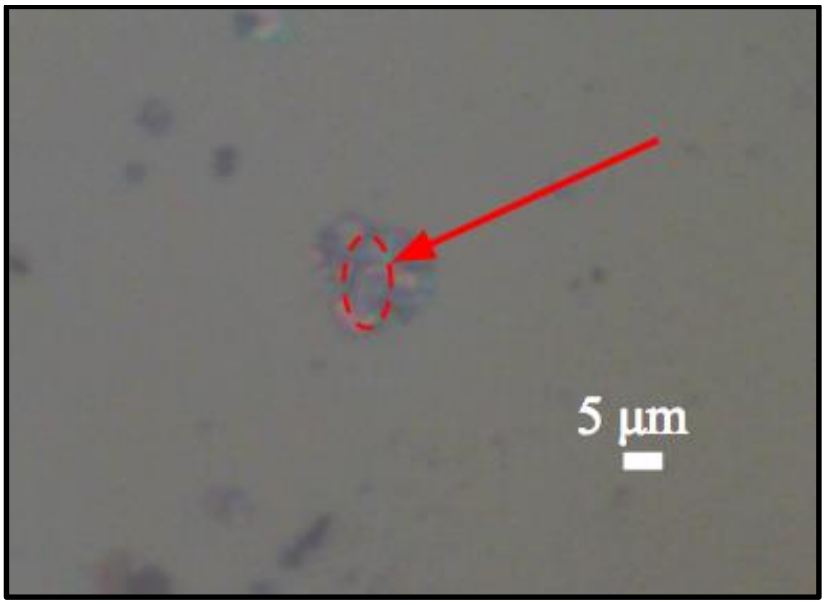

Figure 34: Spot 7 on the BiI_3 flake measured on March 22, 2019

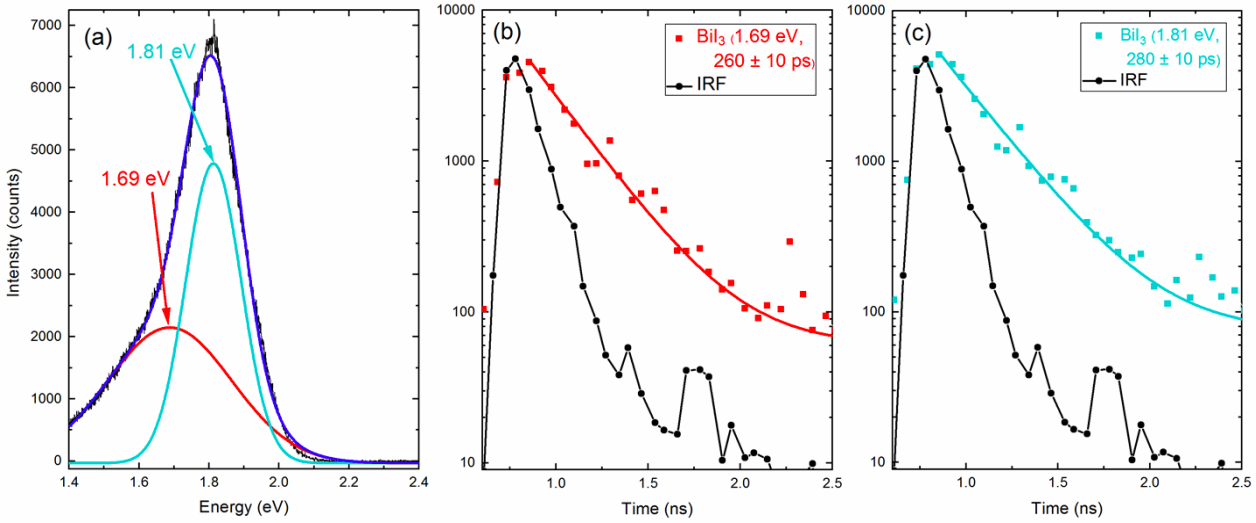

Figure 35: a) Spectra and b) time-decay from spot 7 in Figure 34

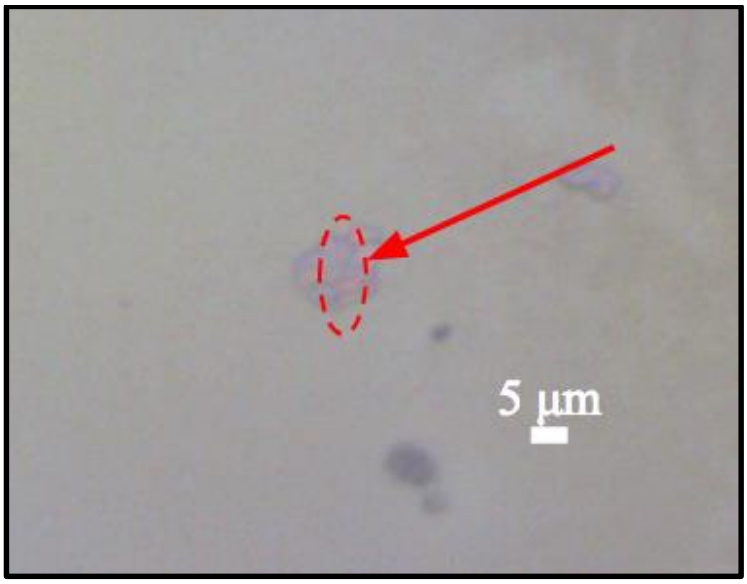

Figure 36: Spot 8 on the BiI_3 flake measured on March 22, 2012

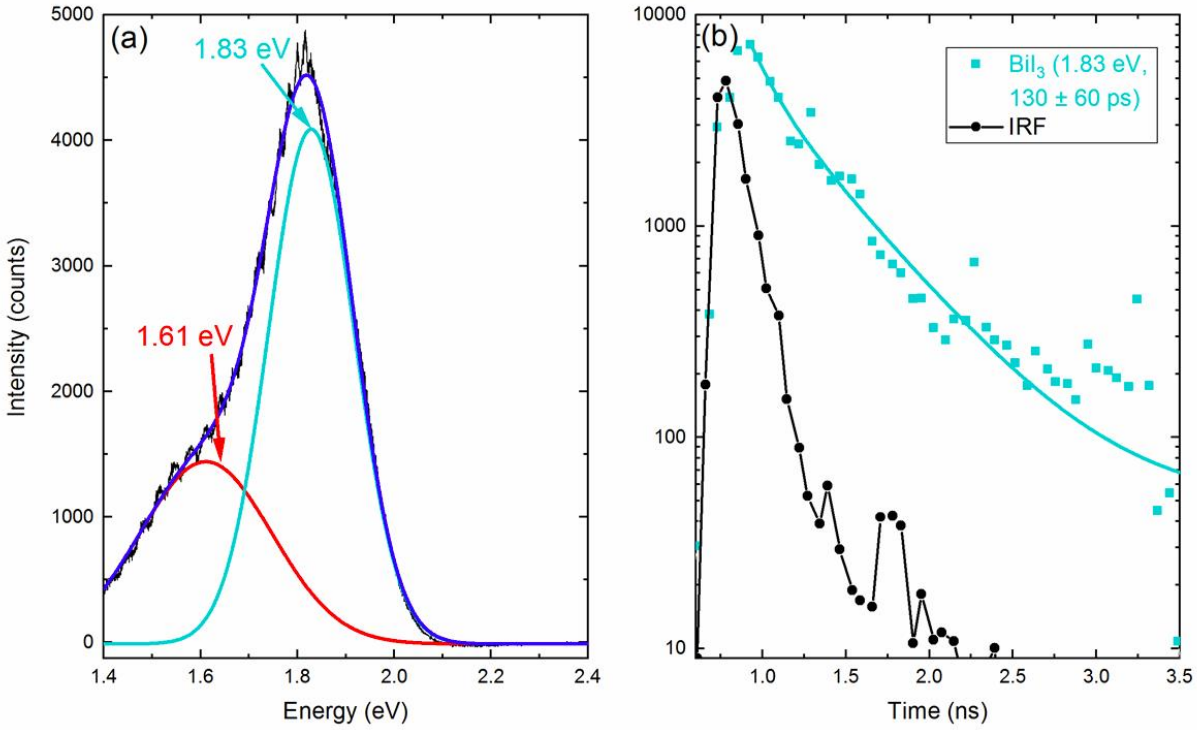

Figure 37: a) Spectra and b) time-decay from spot 8 displayed in Figure 36

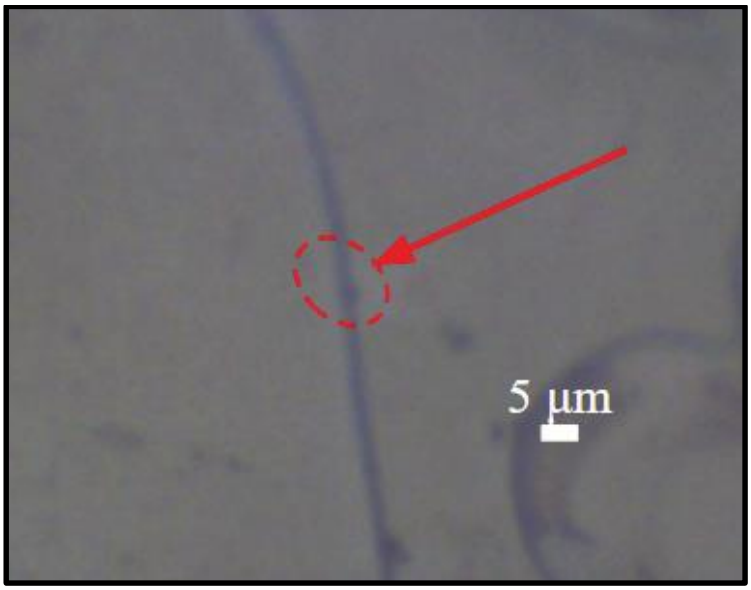

Figure 38: Spot 9 on the BiI_3 flake measured on March 22, 2012

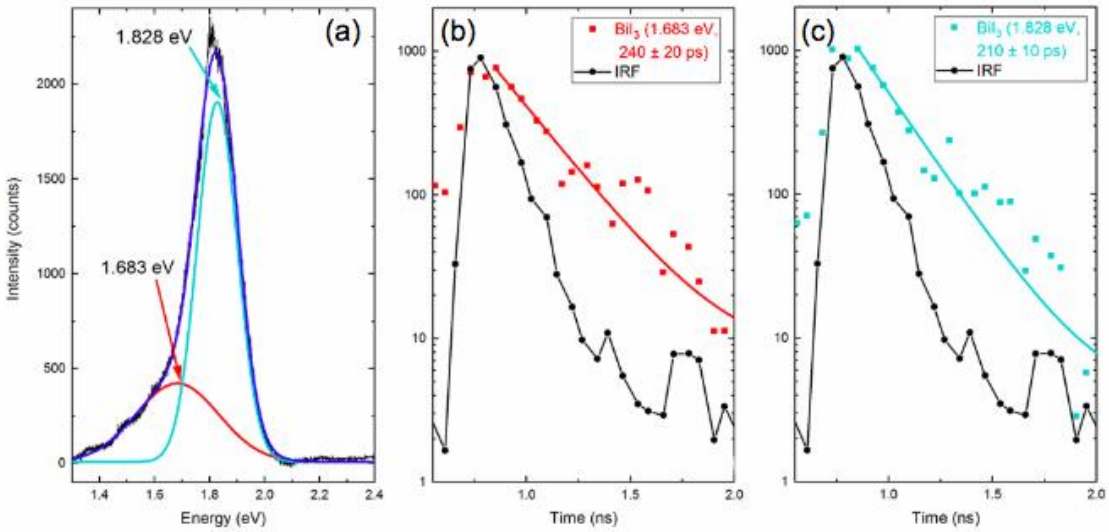

Figure 39: a) Spectra and b) time-decay from spot 9 displayed in Figure 38

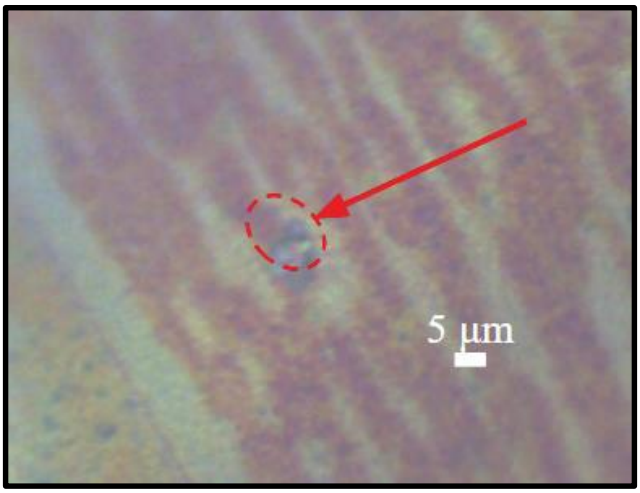

Figure 40: Spot 10 on the BiI_3 flake measured on March 22, 2012

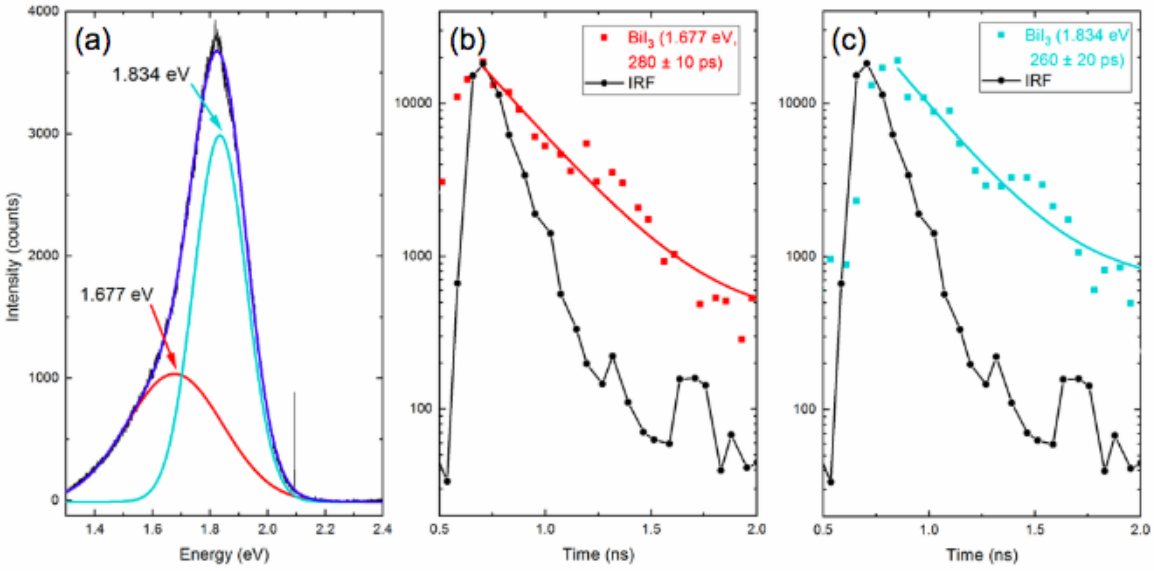

Figure 41: a) Spectra, b) time-decay at 1.677 eV and, c) time-decay at 1.83 eV from spot 10 displayed in Figure 40